Karuppiah, V., Ranaghan, K., Leferink, N. G. H., Johannissen, LO., Shanmugam, M., Cheallaigh, A. N., Bennett, N. J., Kearsey, L. J., Takano, E., Gardiner, J. M., Van der Kamp, M., Hay, S., Mulholland, A., Leys, D., & Scrutton, NS. (2017). Structural basis of catalysis in the bacterial monoterpene synthases linalool synthase and 1,8-cineole synthase. *ACS Catalysis*, *7*(9), 6268-6282. https://doi.org/10.1021/acscatal.7b01924

Peer reviewed version

Link to published version (if available):
10.1021/acscatal.7b01924

Structural basis of catalysis in the bacterial monoterpene synthases linalool synthase and 1,8-cineole synthase

Vijaykumar Karuppiah,[†] Kara E. Ranaghan,[‡] Nicole G. H. Leferink,[†] Linus O. Johannissen,[†] Muralidharan Shanmugam,[†] Aisling Ní Cheallaigh,[†] Nathan J. Bennett,[†] Lewis J. Kearsey,[†] Eriko Takano,[†] John M. Gardiner,[†] Marc W. van der Kamp,[‡] Sam Hay,[†] Adrian J. Mulholland,[‡] David Leys[†] and Nigel S. Scrutton[*,†]

[†]BBSRC/EPSRC Manchester Synthetic Biology Research Centre for Fine and Specialty Chemicals (SYNBIOCHEM), Manchester Institute of Biotechnology, School of Chemistry, Faculty of Science and Engineering, University of Manchester, 131 Princess Street, Manchester M1 7DN, U.K.

[‡]Centre for Computational Chemistry, School of Chemistry, University of Bristol, Cantock's Close, Bristol BS8 1TS, U.K.

ABSTRACT

Terpenoids form the largest and stereochemically most diverse class of natural products, and there is considerable interest in producing these by biocatalysis with whole cells or purified enzymes, and by metabolic engineering. The monoterpenes are an important class of terpenes and are industrially important as flavours and fragrances. We report here structures for the recently discovered *Streptomyces clavuligerus* monoterpene synthases linalool synthase (bLinS) and 1,8-cineole synthase (bCinS) and show that these are active biocatalysts for monoterpene production using biocatalysis and metabolic engineering platforms. In metabolically engineered monoterpene-producing *E. coli* strains use of bLinS leads to 300-fold higher linalool production compared with the corresponding plant monoterpene synthase. With bCinS, 1,8-cineole is produced with 96% purity compared to 67% from plant species. Structures of bLinS and bCinS, and their complexes with fluorinated substrate analogues, show that these bacterial monoterpene synthases are similar to previously characterised sesquiterpene synthases. Molecular dynamics simulations suggest that these monoterpene synthases do not undergo large-scale conformational changes during the reaction cycle making them attractive targets for structured-based protein engineering to expand the catalytic scope of these enzymes towards alternative monoterpene scaffolds. Comparison of the bLinS and bCinS structures indicates how their active sites steer reactive carbocation intermediates to the desired acyclic linalool (bLinS) or bicyclic 1,8-cineole (bCinS) products. The work reported here provides the analysis of structures for this important class of monoterpene synthase. This should now guide exploitation of the bacterial enzymes as gateway biocatalysts for the production of other monoterpenes and monoterpenoids.

KEYWORDS: monoterpene synthase, monoterpenoids, sesquiterpene synthase, terpenes, protein crystallography, molecular dynamics simulations

GRAPHICAL ABSTRACT

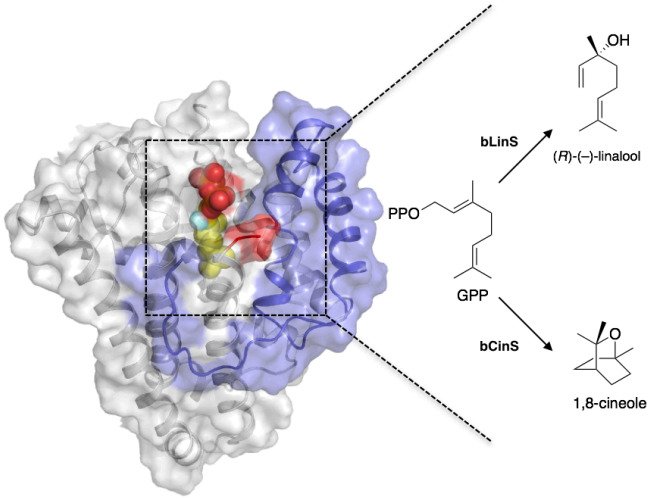

INTRODUCTION

Terpenoids are the most abundant and largest class (>75000) of natural products. Most are commonly found in plants and their biological roles range from interspecies communication to intracellular signaling and defense against predatory species[1]. Their use is wide ranging as pharmaceuticals, herbicides, flavorings, fragrances and biofuels[2]. Despite the commercial interest in terpenoids, efforts to produce these in high yields have been hampered by lack of availability of sufficiently robust and high activity terpene synthase enzymes, although efforts to synthesise terpenoids by synthetic biology routes have gathered pace in the recent years[3-8].

Terpenoids are synthesised from the isoprene building blocks dimethylallyl pyrophosphate (DMAPP) and isopentenyl pyrophosphate (IPP). Combination of DMAPP and IPP generates pyrophosphate substrates of varying carbon lengths, which are then utilised by terpene cyclases to produce either monoterpenes (C10), sesquiterpenes (C15), diterpenes (C20) and others. Geranyl pyrophosphate (GPP), the substrate used by monoterpene synthases is formed by coupling one molecule of DMAPP with IPP, while farnesyl pyrophosphate (FPP), the substrate for sesquiterpenes, is synthesised by coupling three individual isoprene precursors[9].

The class I terpene synthases share a common α-helical fold and use a cluster of three Mg^{2+} ions to assist with substrate ionisation and release of the pyrophosphate moiety (PP_i). This generates a reactive allylic carbocation and triggers a cyclisation cascade that likely involves multiple carbocation intermediates[10]. In many cases, substrate and Mg^{2+} binding lead to a closed active site conformation, which guides substrate

orientation and protects the carbocation intermediates from premature quenching[11]. The exact architecture and mobility of the active site is thought to control the cyclisation cascade to the final carbocation intermediate with high fidelity. The latter is usually subject to deprotonation or addition of a water molecule, leading to formation of a single product. However, some natural terpene synthases and engineered variant forms have been shown to form multiple reaction products[12-13].

To date, available crystallographic structures for the monoterpene cyclases/synthases (mTC/S) that accept GPP as the substrate has been derived only for plant enzymes. Structures have been reported for bornyl diphosphate synthase (*Salvia officinalis)*[14], limonene synthase (*Mentha spicata*[15] and *Citrus sinensis*)[16-17], 1,8-cineole synthase (*Salvia fruticosa*)[18] and γ-terpinene synthase (*Thymus vulgaris*)[19]. Without exception, plant mTC/S contain two domains: a C-terminal α-helical catalytic domain that belongs to the class I terpenoid fold, and a N-terminal α-barrel domain with unclear function and appears to be relictual. Though the overall sequence conservation is low, the structure of the α-helical fold is highly conserved. The active site has two conserved regions, the aspartate rich (DDXX(X)(D,E)) motif and the NSE (NDXXSXX(R,K)(E,D)) triad, required for binding three catalytically essential Mg^{2+} ions. Structures of bornyl diphosphate synthase and limonene synthases have been solved in complex with substrate analogues. In each case, GPP-analogues bind with their pyrophosphate moieties coordinated by the Mg^{2+} ions and a network of residues that are proposed to assist with catalysis.

Recent reports have shown that terpene synthases are also widely distributed in bacteria, but the majority of these accept FPP as substrate and produce

sesquiterpenes[20-21]. Ohnishi and coworkers characterised two bacterial mTC/S from *Streptomyces calvuligerus*, namely 1,8-cineole synthase[22] and linalool/nerolidol synthase, which can accept either GPP and FPP as substrate, leading to linalool and nerolidol products, respectively[23]. Heterologous expression of these enzymes in *Streptomyces avermitilis* resulted in 1,8-cineole synthase (bCinS) producing 1,8-cineole, and linalool/nerolidol synthase (bLinS) producing only linalool indicating that bLinS is likely to function only as a mTC/S in this host[20]. The sequences of both bCinS and bLinS reveal they comprise ~330 amino acids in a single catalytic domain and lack the additional N-terminal α-barrel domain characteristic of plant enzymes. Surprisingly, no closely related homologs of both enzymes have been found in other bacteria[24]. The bacterial mTC/S 2-methylisoborneol synthase is present in many bacteria. It accepts 2-methyl-GPP as substrate to produce 2-methylisoborneol. Unlike the bacterial mTC/S reported here, 2-methylisoborneol synthase has a considerably longer amino acid sequence (~400-500) and crystal structures have revealed a N-terminal proline-rich domain that is disordered along with a class I terpenoid fold C-terminal domain[25].

Linalool is mainly used as a fragrance material in 60-80% of perfumed hygiene products. It is widely used in cosmetic products like perfumes, lotions, soaps and shampoos and also in non-cosmetic products like detergents and cleaning agents. Furthermore, during the manufacturing process of Vitamin E, linalool is a vital intermediate. As an important ingredient in a wide range of commercial products, the worldwide use of linalool exceeds 1000 metric tonnes per annum[26]. Both *R* and *S* isomers of linalool are found in nature with *R*-(–)-linalool being the most widely distributed in plant and flower extracts. To our knowledge, for industrial use as a

fragrance, the isomeric mixture is used. 1,8-cineole (also called eucalyptol) is used as a flavoring in food products, in cosmetics and also has medicinal properties[27].

This study integrates synthetic biology with biocatalysis and analysis of enzyme structures and mechanisms. Here we describe high-resolution crystal structures of bLinS and bCinS from *Streptomyces calvuligerus*, and complexes with fluorinated substrate analogues. These structures define the active site architectures required to steer reactive carbocation intermediates to the desired product outcomes. Expression of bLinS and bCinS in *E. coli* monoterpene producing strains leads to improved production of linalool and 1,8-cineole compared with plant monoterpene synthases and the structures help to both rationalise product outcomes and guide future exploitation of these enzymes in monoterpene/monoterpenoid production.

EXPERIMENTAL SECTION

Expression and Purification of bCinS and bLinS

The full-length genes coding for 1,8-Cineole synthase (bCinS; WP_003952918) and Linalool synthase (bLinS; WP_0003957954) from *Streptomyces clavuligerus* ATCC 27064 were codon optimised and synthesised from GeneArt (Life Technologies). The genes were amplified using PCR and sub-cloned into pETM11 vector digested with NcoI and XhoI using Infusion cloning (Clontech). The final construct coded for either 1,8-Cineole synthase (bCinS) or Linalool synthase (bLinS) with a 6X-His tag followed by a TEV protease cleavage site at the N-terminus. The expression and purification method explained below was identical for both the proteins. The plasmid was transformed into *E. coli* ArcticExpress (DE3) cells (Agilent) and a few colonies

were inoculated into 100 ml 2X-YT media containing 40 μg/ml of kanamycin and 20 μg/ml of gentamycin and grown for 3-4 h at 37 °C. The culture was diluted into 3 litres of fresh 2X-YT media containing 40 μg/ml of kanamycin and allowed to grow at 37 °C until the OD at 600 nm reached 0.6-0.8. At this stage, the temperature was reduced to 16°C and 0.1 mM Isopropyl β-D-1-thiogalactopyranoside (IPTG) was added and incubated for 14-18 h. The cells were harvested by centrifugation at 6000 g for 10 min and the pellet was resuspended in buffer A (25 mM Tris pH 8.0, 150 mM NaCl, 1 mM DTT, 4 mM $MgCl_2$ and 5% (v/v) glycerol). The cells were lysed by sonication and the debris was removed by centrifugation at 30,000 g for 30 min. The supernatant was filtered through a 0.2 μm filter and loaded onto a 5 ml HisTrap column (GE Healthcare) pre-equilibrated with buffer A. The column was washed with buffer A containing 10 mM imidazole (pH 8.0) and increasing up to 40 mM imidazole by step gradients with 3 column volume for each concentration. Increasing the concentration of imidazole to 200-500 mM eluted the protein. The purified protein was desalted using a Centripure P100 column (emp Biotech GmbH) equilibrated with buffer A. To remove the His tag, TEV protease was added (1:1000 (w/w)) to the protein and incubated at 4 °C with gentle mixing for 24 h. The TEV protease was removed by passing the protein mixture through a 5 ml HisTrap column and the flow through was collected. The His-tag removed protein was concentrated and loaded onto a Hiload Superdex (26/60) S75 column (GE Healthcare) pre-equilibrated with buffer A. Pure fractions from the gel filtration column were concentrated to 13-15 mg/ml and stored at -80 °C as aliquots. Samples for EPR experiments were prepared as explained above except buffer A was lacking $MgCl_2$.

Biotransformations

Biotransformation reactions (0.25 ml) were prepared using buffer A and setup in glass vials containing 2 mM GPP and 20 μM of bCinS or bLinS. The vials were incubated at 25°C with gentle shaking for 16 h. The vials were cooled to 4°C and 0.25 ml of ethyl acetate containing 0.01% (v/v) *sec*-butyl benzene as internal standard was added. The samples were vortexed for 2 min and then spun at 18,000 g for 5 min. Supernatant fractions containing the ethyl acetate layer were removed and dried over anhydrous magnesium sulfate. Samples were analysed by GC-MS.

Monoterpenoid Production in *E.coli*

Both bLinS and bCinS genes, including RBS, were amplified from their respective pETM-11 expression vectors using primers pET_IF_Fw (5'-CAT CCC CAC TAC TGA GAA TC-3') and pET_IF_Rv (5'- GGT GGT GGT GCT CGA GTT A-3') and cloned using InFusion (Takara) into plasmid pGPPSmTC/S15 (**Table S1**), which was PCR linearised using the primer pair Vector_IF_Fw (5'-TAA CTC GAG CAC CAC CAC CAC C-3') and Vector_IF_Rv (5'-TCA GTA GTG GGG ATG TCG TAA TCG-3') resulting in plasmids pGPPSmTC/S38 and pGPPSmTC/S39, respectively (**Table S1**). Correct insertion was confirmed by automated sequencing (Eurofins).

For monoterpenoid production, the pGPPSmTC/S plasmids were co-transformed with pMVA into *E. coli* DH5α and grown as described before[3]. Briefly, expression strains were inoculated in terrific broth (TB) supplemented with 0.4% glucose in glass screw capped vials, and induced for 72 h at 30°C with 50 μM IPTG and 25 nM anhydro-tetracycline. A 20% *n*-nonane layer was added to capture the volatile terpenoids products. After induction, the nonane overlay was collected, dried over anhydrous

$MgSO_4$ and mixed at a 1:1 ratio with ethyl acetate containing 0.1% (v/v) *sec*-butyl benzene as internal standard.

GC-MS Analysis

Samples were injected onto an Agilent Technologies 7890B GC equipped with an Agilent Technologies 5977A MSD. The products were separated on a DB-WAX column (30 m x 0.32 mm i.d., 0.25 μm film thickness, Agilent Technologies). The injector temperature was set at 240°C with a split ratio of 20:1 (1 μl injection). The carrier gas was helium with a flow rate of 1 ml/min and a pressure of 5.1 psi. The following oven program was used: 50 °C (1 min hold), ramp to 68 °C at 5 °C/min (2 min hold), and ramp to 230 °C at 25 °C/min (2 min hold). The ion source temperature of the mass spectrometer (MS) was set to 230 °C and spectra were recorded from m/z 50 to m/z 250. Compound identification was carried out using authentic standards and comparison to reference spectra in the NIST library of MS spectra and fragmentation patterns as described previously[3].

GC Analysis

To determine the chirality of linalool and nerolidol produced by bLinS, samples were analysed by gas chromatography on an Agilent Technologies 7890A GC system equipped with an FID detector, a 7693 autosampler and a CP-Chirasil-DEX-CB column (25 m x 0.25 mm i.d., 0.25 μm film thickness). The biotransformation samples and isomers of linalool and nerolidol standards were analysed using GC. In this method, the injector temperature was at 180°C and 1 μl of sample was injected split-less. The carrier gas was helium with a flow rate of 1 ml/min and a pressure of 11.3 psi. For nerolidol containing samples, the program began at a temperature of

70°C and then increased to 150 °C at 8°C/min (2 min hold). This was followed by an increase in temperature to 190 °C at 10 °C/min (3 min hold). For linalool containing samples, the program began at a temperature of 70 °C which was then increased to 90 °C at 8°C/min. This was followed by an increase in temperature to 150°C at a rate of 2 °C/min and then to 190 °C at 40 °C/minute (1 min hold). The FID detector was maintained at a temperature of 200°C with a flow of hydrogen at 30 ml/min.

Chemical Synthesis of Fluorinated Substrate Analogues

Unless otherwise stated, all reactions were carried out in oven-dried glassware. Reactions were monitored by Thin Layer Chromatography (TLC) on silica gel 60 F_{254} plates, visualised with phosphomolybdic acid stain (10 g Phosphomolybdic acid in 100 ml ethanol). Column chromatography was performed on Merck silica Gel 60 (particle size 40-63µm). ^{1}H NMR, ^{13}C NMR, ^{31}P and ^{19}F spectra were obtained using a combination of 400 MHz and 500 MHz spectrometers and are reported as chemical shift on the parts per million scale. Multiplicity abbreviated (br = broad, s = singlet, d = doublet, dd = double doublet, t = triplet, m = multiplet, *etc*.) and coupling constants were obtained in Hertz. Assignments were aided by COSY and HSQC. All mass spectrometry results are reported as the mass to charge ratio and are reported with % abundance against the base peak (100 %).

Synthesis of 2-fluorogeraniol and 2-fluoronerol: Sodium hydride (538 mg, 60% dispersion, 13.5 mmol) was washed with petroleum ether and suspended in THF (40 ml). The suspension was cooled to 0 °C and a solution of the ethyl (diethoxyphosphoryl) fluoroacetate (2.48 ml, 12.2 mmol) in THF (13.4 ml) was added dropwise over 10 min. The reaction was stirred for 30 min before adding 6-methyl-5-

hepten-2-one (1.5 ml, 10.2 mmol) dropwise over 30 min. The reaction was stirred overnight at room temperature. The reaction was cooled back to 0 °C and quenched by pouring on to ice water. The product was extracted with diethyl ether (3 x 30 ml), dried over $MgSO_4$ and then reduced to dryness. The crude product was then dissolved in THF (64 ml), cooled to 0 °C and $LiAlH_4$ (541 mg, 14.3 mmol) was added. The reaction was stirred at room temperature for 3 hours then quenched with the addition of saturated aqueous NH_4Cl. The solution was extracted with diethyl ether (3 x 30 ml) and the subsequent combined organic phases were washed with brine (30 ml). The product was purified by column chromatography (hexane/diethyl ether, 95/5, v/v) to give 2-fluorogeraniol (783 mg, 41%) and 2-fluoronerol (856 mg, 45%) with a total yield of 86%[25, 28] (**Scheme S1**). **2-fluorogeraniol**: ^{1}H NMR (400 MHz, $CDCl_3$) δ 5.17 – 5.05 (m, 1H, H7), 4.24 (dd, *J* = 22.3, 3.2 Hz, 2H, H1), 2.10 (m, 4H, H5, H6), 1.68 (s, 3H, H4), 1.67 (d, *J* = 2.9 Hz, 3H, H9/10), 1.61 (s, 3H, H9/10). ^{13}C NMR (101 MHz, $CDCl_3$) δ 132.2, 123.6, 116.1 (d, J = 16.2 Hz), 58.2 (d, J = 29.3 Hz), 29.8 (d, J = 7.07 Hz), 25.9 (d, J = 4.0 Hz), 25.7, 17.6, 15.4 (d, J = 6.01 Hz). ^{19}F NMR (471 MHz, $CDCl_3$) δ -121.3 (t, *J* = 22.4 Hz) (**Figure S1a-e**). **2-fluoronerol:** ^{1}H NMR (400 MHz, $CDCl_3$) δ 5.16 – 5.02 (m, 1H, H7), 4.19 (dd, *J* = 22.9, 5.3 Hz, 2H, H1), 2.16 – 2.00 (m, 4H, H5, H6), 1.70 (s, 3H, H4), 1.60 (s, 3H, H9/10), 1.57 (s, 3H, H9/10). ^{13}C NMR (101 MHz, $CDCl_3$) δ 133.3, 123.5, 115.9 (d, J = 14.1 Hz) , 58.0 (d, J = 29.2 Hz), 31.9 (d, J = 5.1 Hz), 26.6 (d, J = 5.1 Hz), 25.8, 17.9, 13.7 (d, J = 9.1 Hz). ^{19}F NMR (471 MHz, $CDCl_3$) δ –119.4 (t, *J* = 22.6 Hz) (**Figure S2a-e**).

Synthesis of 2-fluorogeranyl pyrophosphate (FGPP) and 2-fluoroneryl pyrophosphate (FNPP): Acetonitrile (60 ml) was added to 2-fluorogeraniol or 2-fluoronerol (400 mg, 2.3 mmol). To this, trichloroacetonitrile (2 ml) was added

followed by $H_3PO_4(Et_3N)_2$ salt (2.1 g). The reaction was stirred overnight. It was then poured on to diethylether (50 ml) and washed with concentrated aqueous ammonia (3 x 100 ml). The ammonia washes were combined and washed once with diethyl ether (50 ml). The aqueous phase was reduced to dryness. The crude product was loaded on to a silica gel column and the starting material was recovered using petroleum ether/diethyl ether (9/1, v/v). The eluent system was then switched to propanol/concentrated aqueous ammonia/water (7/2/1, v/v/v) to isolate mono and pyrophosphate derivatives (**Scheme S1**). When 2-fluorogeraniol was used, 2-fluorogeranyl monophosphate (93 mg, 0.37 mmol, 16%) and 2-fluorogeranyl pyrophosphate (74 mg, 0.2 mmol, 10%) were obtained. When 2-fluoronerol was used, 2-fluoroneryl monophosphate (117 mg, 0.47 mmol, 20%) and 2-fluoro neryl pyrophosphate (200 mg, 0.54 mmol, 27%) were obtained. **2-fluorogeraniol pyrophosphate**: ^{1}H NMR (500 MHz, D_2O) δ 5.29 – 5.15 (m, 1H, H7), 4.59 (dd, *J* = 23.6, 6.2 Hz, 2H, H1), 2.22 – 2.09 (m, 4H, H5, H6), 1.72 (d, *J* = 2.8 Hz, 3H, H4), 1.69 (s, 3H, H9/10), 1.62 (s, 3H, H9/10). ^{13}C NMR (126 MHz, D_2O) δ 133.9 (s), 123.7 (s), 119.5 (d, *J* = 15.0 Hz), 60.9 (dd, *J* = 31.6, 5.0 Hz), 29.1 (d, *J* = 6.4 Hz), 25.1 (s), 24.8 (s), 16.9 (s), 14.6 (d, *J* = 4.9 Hz). ^{31}P NMR (162 MHz, D_2O) δ –8.37 (d, *J* = 21.5 Hz), –10.95 (d, *J* = 21.6 Hz). ^{19}F NMR (471 MHz, D_2O) δ -120.44 (t, *J* = 23.6 Hz). HRMS ESI $C_{10}H_{18}FO_7P_2$ $[M–H]^-$ calculated: 331.0512, found: 331.0517 (**Figure S3a-g**). Data was found to be in accordance with the literature[16, 29]. **2-fluoronerol pyrophosphate**: ^{1}H NMR (400 MHz, D_2O) δ 5.14 – 5.06 (m, 1H, H7), 4.50 (dd, *J* = 23.6, 6.1 Hz, 2H, H1), 2.07 (br s, 4H, H5, H6), 1.62 (s, 6H, H4, H9/10), 1.54 (s, 3H, H9/10). ^{13}C NMR (126 MHz, D_2O) δ 134.3 (s), 123.3 (s), 119.1 (d, *J* = 13.2 Hz), 60.4 (dd, *J* = 31.0, 4.3 Hz), 30.8 (d, *J* = 4.6 Hz), 25.7 (d, *J* = 2.7 Hz), 24.8 (s), 16.9 (s), 12.8 (d, *J* = 8.6 Hz) ^{31}P NMR (162 MHz, D_2O) δ –7.64 (d, *J* = 21.4 Hz), –10.93 (d, *J*

= 20.9 Hz) ^{19}F NMR (471 MHz, D_2O) δ –119.13 (t, *J* = 23.1 Hz). HRMS ESI $C_{10}H_{18}FO_7P_2$ $[M–H]^-$ calculated: 331.0512, found: 331.0517 (**Figure S4a-h**). Data was found to be in accordance with the literature[16, 29].

Crystallisation of bCinS and bLinS

Crystallisation trials containing 200 nl of protein and 200 nl of precipitant solution were setup in 3-well swissci plates using a mosquito robot (TTP Labtech). Five commercial screens namely Morpheus I and II, JCSG+, PACT premier and SG1 (Molecular Dimensions Ltd) were used in initial trails. For both enzymes, three distinct samples were screened: the *apo*-enzyme, the enzyme in presence of 2 mM FGPP, and the enzyme in presence of 2 mM FNPP. The bCinS-FNPP crystallised in Morpheus II A4 condition (90mM of LiNaK (0.3M lithium sulphate, 0.3M sodium sulphate, 0.3 M potassium sulphate), 0.1M of buffer system 4 (1M MOPSO, 1M Bis-Tris) pH 6.5 and 50% precipitant mix 8 (10% PEG 20000, 50% trimethyl propane, 2% NDSB 195)). The bLinS-FGPP crystallised in Morpheus D7 condition (0.12 M Alcohols (0.2M 1,6-hexanediol, 0.2M 1-nutanol, 0.2M 1,2-propanediol, 0.2M 2-propanol, 0.2M 1,4-butanediol, 0.2M 1,3-propanediol), 0.1 M Buffer System 2 (1.0M sodium HEPES, MOPS (acid)) pH 7.5 and 50% v/v precipitant Mix 3 (40% v/v glycerol, 20% w/v PEG 4000)). The *apo*-LinS crystallised in SG1 E2 condition (25% w/v PEG3350). Although *apo*-bCinS crystallised, optimisation of growth conditions failed to produce single crystals of sufficient size for further study. In an attempt to obtain the bCinS-FGPP structure, bCinS-FNPP crystals were soaked overnight in presence of 2mM FGPP prior to cryo-cooling. The *apo*-bLinS crystals were cryo-protected by soaking in mother liquor supplemented with 20% glycerol. For all FGPP and FNPP complexes, the ligands were included in the cryo-solution.

Structure Solution

All data were collected at Diamond Light Source (DLS). Diffraction images were integrated and scaled by xia2[30] automated data processing pipeline, using XDS[31] and XSCALE. Crystals of bCinS contained two molecules in the asymmetrical unit and belonged to P1 space group. Crystals of bLinS belonged to the tetragonal system (spacegroup I4) and also contained two molecules in asymmetrical unit. The bLinS structures (*apo*-bLinS and bLinS-FGPP) were solved by molecular replacement using the Pentalenene synthase structure (PDB 1PS1[32]) as the search model in Phaser[33]. The bCinS-FNPP structure was solved by model replacement using the *apo*-bLinS structure as the search model. The *apo*-bLinS, bLinS-FGPP, bCinS-FNPP and bCinS-FNPP/FGPP models were built using Autobuild in Phenix[34]. The structures were completed using iterative rounds of manual model building in coot[35] and refinement in phenix.refine[36]. The structures were analysed using PDB_REDO[37] and validated using molprobity tools[38]. The refinement statistics are provided in **Table 1**. The atomic coordinates and structure factors have been deposited in the Protein Data Bank with accession codes 5NX4, 5NX5, 5NX6 and 5NX7.

Table 1: X-ray data collection and refinement statistics

	bLinS (apo)	bLinS-FGPP	bCinS-FNPP	bCinS-FNPP/FGPP
Data collection				
Space group	I4	I4	P1	P1
Unit cell dimensions	a=b=140.15 Å, c=87.18 Å; α=β=γ=90°	a=b=139.37 Å, c=86.06 Å; α=β=γ=90°	a=60.81 Å, b=60.83 Å, c=64.10 Å; α=90.04°, β=92.89°, γ=101.98°	a=60.75 Å, b=60.83 Å, c=64.26 Å; α=92.67°, β=89.98°, γ=101.77°
X-ray source	DLS I04-1	DLS I04	DLS I04	DLS I04
Wavelength (Å)	0.92819	0.99	0.99	0.9795
Resolution range (Å)	50.90-2.38 (2.42-2.38)	36.62-1.82 (1.85-1.82)	32.27-1.63 (1.66-1.63)	64.19-1.51 (1.53-1.51)
Multiplicity	4.5 (3.9)	6.8 (6.9)	1.8 (1.8)	2 (2)
I/σ I	14.6 (1.7)	18.2 (1.4)	6.7 (1.2)	10 (2.1)
Completeness (%)	99.7 (99.7)	100 (100)	96 (94.6)	95.9 (93.4)
R_{merge}	0.082 (0.766)	0.057 (1.371)	0.09 (0.639)	0.035 (0.315)
R_{meas}	0.093 (0.889)	0.062 (1.483)	0.127 (0.904)	0.047 (0.428)
R_{pim}	0.043 (0.44)	0.024 (0.563)	0.09 (0.639)	0.032 (0.287)
$CC_{1/2}$	0.998 (0.576)	0.999 (0.51)	0.987 (0.479)	0.999 (0.824)
Total observations	152818 (6641)	502331 (25222)	193529 (9539)	270436 (13510)
Total unique	33849 (1697)	73739 (3654)	107492 (5258)	136704 (6737)
Refinement				
R-work	0.1850	0.1667	0.1662	0.1492
R-free	0.2240	0.1950	0.20	0.1830
RMS (bonds)	0.002	0.009	0.013	0.008
RMS (angles)	0.45	0.94	1.15	0.96
Average B-factor (Å^2)	52.5	42.8	24.8	27.8
Ramachandran plot				
Favored	98.94	99.29	98.98	98.45
Allowed	1.06	0.71	1.02	1.35
Outliers	0	0	0	0.2

EPR Spectroscopy

Electron Paramagnetic Resonance (EPR) measurements were carried out using a Bruker ELEXSYS-500 X-band EPR spectrometer operating in both cw and pulsed modes, equipped with an Oxford variable-temperature unit and ESR900 cryostat with Super High-Q resonator. All EPR samples were prepared in the quartz capillary tubes (outer diameter; 4.0 mm, inner diameter 3.0 mm) and frozen in liquid N_2. The X-band EPR tubes were then transferred into the EPR probe head, which was pre-cooled to 20 K. The low-temperature EPR spectra were measured at 20 K as a frozen solution. A microwave power of 36 dB (50 mW) and modulation of 5 G appear to be optimal for recording the EPR spectrum of the bLinS and bCinS protein samples prepared using various ratio of protein to Mn^{2+} concentration in the presence of 10-fold excess of FGPP. The concentrations of the proteins (bLinS and bCinS) and FGPP in all the samples were 0.400 mM and 1.5 mM respectively, whereas the ratio to the Mn^{2+}

concentration was systematically varied from 1 to 6. The low temperature EPR spectra were acquired using the following conditions: sweep time of 84 s, microwave power of 50 mW, time constant of 41 ms and modulation amplitude of 5 G. All the spectra have been normalised to account for the different numbers of scans accumulated for each sample. The data analysis was performed using EasySpin toolbox for the Matlab program package.

Simulations of *Apo*-bCinS and bLinS

Molecular dynamics (MD) simulations of *apo*-bCinS and bLinS were carried out in AMBER14 using the CHARMM27 force field[39-40]. The protonation states of titratable residues were estimated using the PDB2PQR server with proPKA, and the enzymes were solvated using a box of minimum 12 Å around the protein with counter-ions added. Two sets of isothermal-isobaric ensemble (NPT) MD simulations were performed at 298 K for each enzyme, using different starting velocities, following the system setup. Langevin dynamics was used for temperature control (collision frequency of 5 ps^{-1} for equilibration and 2 ps^{-1} for production), and pressure was controlled by coupling to an external bath (AMBER14 default settings) for NPT conditions. The system setup consisted of: (i) energy minimisation of the solvent; (ii) 50 ps of (NPT) solvent equilibration; (iii) energy minimisation of the entire system with positional restraints of 5 kcal mol^{-1} $Å^{-2}$ applied to all Cα atoms; (iv) canonical ensemble (NVT) thermalisation to 298 K over 20 ps with positional restraints of 5 kcal mol^{-1} $Å^{-2}$ on Cα atoms; (v) 40 ps of NPT equilibration with decreasing restraints on the Cα atoms; (vi) 1 ns unconstrained NPT equilibration; (vii) 100 ns production simulation. Average linkage hierarchical clustering (after alignment of structures

based on Cα positions) was used to identify representative structures to illustrate protein conformational sampling during the simulations.

Simulations of the Ternary Complexes of bCinS with 3 Mg^{2+} Ions and GPP or NPP

The protonation states of titratable residues were estimated using PropKA3.1[41-42] and the enzyme was solvated using a box of TIP3P[43] water molecules (with a minimum buffer or 13 Å around the protein) using the solvate plugin of the VMD package[44]. Counter-ions were added to neutralize the system using autoionize plugin of VMD[44]. The CHARMM27 forcefield[39] was used to describe the protein with parameters for GPP and NPP were adapted from those used for FPP in the work of van der Kamp *et al*.[45]. The position of the GPP or NPP substrate was based on the position of the fluorinated analogue resolved in the crystal structure. Due to the minimal differences in the structure of the inhibitor and substrate (F vs H), the position in the crystal structure was considered a suitable starting point for the simulations. It has been suggested that many terpene cyclase/synthase structures contain substrates bound in unreactive conformations[46-47]; however structures containing the larger and more flexible FPP, the building block for sesquiterpenes are more prevalent than monoterpenes. The parameter set developed by Allner *et al*.[48] was used to describe the three Mg^{2+} ions. The setup of the model consisted of: (i) minimisation of the positions of the hydrogen atoms (all heavy atoms fixed); (ii) minimisation of the solvent (with all protein heavy atoms fixed); (iii) energy minimisation of the entire system with positional restraints of 5 kcal mol^{-1} $Å^{-2}$ applied to all Cα atoms; (iv) canonical ensemble (NVT) thermalisation to 300 K over 20 ps with positional restraints of 5 kcal mol^{-1} $Å^{-2}$ on Cα atoms; (v) thermal equilibration at 300K for 100 ps with

positional restraints of 5 kcal mol^{-1} $Å^{-2}$ on Cα atoms; (vi) 140 ps of NPT equilibration with decreasing restraints on the Cα atoms; (vi) 100 ns production simulation. Two sets of isothermal-isobaric ensemble (NPT) MD simulations were performed at 300 K for each enzyme, repeating steps (iv)-(vi) to obtain 2 models with different initial conditions. MD simulations were carried out on GPUs using the PMEMD code[49] of AMBER16[50]. Langevin dynamics was used for temperature control (collision frequency of 5 ps^{-1} for equilibration and 2 ps^{-1} for production), and pressure was controlled by coupling to an external bath (AMBER16 default settings) for NPT conditions. Average linkage hierarchical clustering (after alignment of structures based on positions of active site residues) was carried out using the CPPTRAJ utility of AMBERTOOLS 16[50] to identify representative structures of the ternary complex over the course of the simulations.

Simulations of the Ternary Complexes of bLinS with 3 Mg^{2+} Ions and GPP or FPP

The models of bLinS were built from the coordinates of chain B of the protein, with positions of the Mg^{2+} ions determined based on alignment with the structures of sesquiterpene synthases aristocholene synthase (ATAS, PDB 4KUX[51]) and Epi-isozizaene synthase (PDB 3KB9[52]). GPP was built into the model based on the position of the phosphate ion observed in the bLinS chain B structure and using the geometry of FGPP observed in the bCinS-FGPP structure. The FPP model was generated based on the position of farnesyl thiolodiphosphate FSPP in ATAS[51]. Some positional restraints were then applied to the Mg^{2+} ions and coordinating protein residues in the NSD and DDXXD motifs in order to form the correct binding pattern. The Mg^{2+} to oxygen atom distance (for Asn218, Ser222, Asp226 and Asp79) was

restrained to a value of 2.3 Å with a force constant k = 20 kcal mol^{-1} $Å^{-2}$. The same procedure as used for the bCinS models was then followed to perform the MD simulations of bLinS with GPP and FPP.

RESULTS AND DISCUSSION

Linalool and 1,8-cineole Production in *E. coli*

Biotransformation reactions showed that purified bLinS and bCinS produced linalool and 1,8-cineole, respectively, when supplied with GPP. No by-products were observed when analysed by GC-MS (**Figure 1**). To investigate the suitability of both enzymes for monoterpenoid production in engineered *E. coli* strains, bLinS and bCinS were inserted in an *E. coli* 'plug-and-play' monoterpenoid production platform, which consists of two gene modules[3]. The first module (pMVA) contains a hybrid mevalonate (MVA) pathway under regulation of IPTG-inducible promoters[53] and the second (plasmid series pGPPSmTC/S, **Table S1**) comprises a refactored, N-terminally truncated geranyl diphosphate synthase (GPPS) gene from *Abies grandis* (AgtrGPPS2) followed by an mTC/S gene (in this case bLinS or bCinS, respectively) under control of a tetracycline-inducible promoter. Strains containing both the pMVA and pGPPS-bLinS or pGPPS-bCinS plasmids, respectively, were grown in a two-phase shake flask system using glucose as the feedstock and *n*-nonane as an organic phase to facilitate product capture. Products accumulated in the organic phase were identified and quantified by GC-MS analysis.

Product profiles and titres obtained with bLinS and bCinS were compared with previously obtained profiles using mTC/S enzymes obtained from plants (**Figure 1**), i.e. LinS from *Artemisia annua* (RLinS_Aa) and CinS from *Salvia fruticosa*

(CinS_Sf), *Arabidopsis thaliana* (CinS_At), and *Citrus unshiu* (CinS_Cu)[3]. Both bacterial enzymes outperformed the plant enzymes: bLinS produced about 300-fold more linalool than RLinS_Aa (363.3 ± 57.9 versus 1.3 mg L_{org}^{-1}). With bCinS, 1,8-cineole was produced in considerably purer form compared to that produced using the plant enzymes. Strains containing bCinS produced 116.8 ± 36.4 mg L_{org}^{-1} (96% pure); this compares to 118.2 mg L_{org}^{-1} (67% pure) for CinS_Sf, 46.6 mg L_{org}^{-1} (42% pure) for CinS_At, and 18.2 (63% pure) for CinS_Cu for the strains containing the corresponding plant CinS enzymes.

As well as GPP formation catalysed by the heterologous GPPS, the engineered *E. coli* strains also produce the sesquiterpene precursor farnesyl diphosphate (FPP) from native host encoded enzymes[54]. Strains containing bLinS were able to convert FPP to nerolidol (159.1 ± 7.3 mg L_{org}^{-1}), indicating that bLinS acts as both a monoterpene and sesquiterpene synthase. We demonstrated that bLinS makes *R*-(–)-linalool and *trans*-nerolidol with GPP and FPP, respectively (**Figure S5a-f**). In contrast, no sesquiterpene products were detected with *E. coli* strains containing bCinS indicating it is restricted to the production of monoterpene products. With each of the strains, geraniol and farnesol (and their derivatives) were detected in organic overlays of cultures alongside the expected terpenoids. An unidentified endogenous *E. coli* pathway has previously been shown to convert both GPP and FPP into geraniol and farnesol respectively[3], which are subsequently converted into oxidative by-products by endogenous dehydrogenation and isomerisation reactions[55]. In particular, *E. coli* PhoA phosphatase was implicated in converting GPP to geraniol[56] and two integral membrane phosphatases (PgpB and YbjG) were shown to convert FPP to farnesol[57].

The reported product profiles and yields suggest that bacterial monoterpene synthases are better suited compared to the corresponding plant enzymes for monoterpenoid production using engineered *E. coli* strains. Armed with this information we set out to determine the structures of bLinS and bCinS, in both ligand-free and complexed with fluorinated substrate analogues, with the objective of informing on mechanism, and guiding future engineering/exploitation in biocatalysis and metabolic engineering programmes.

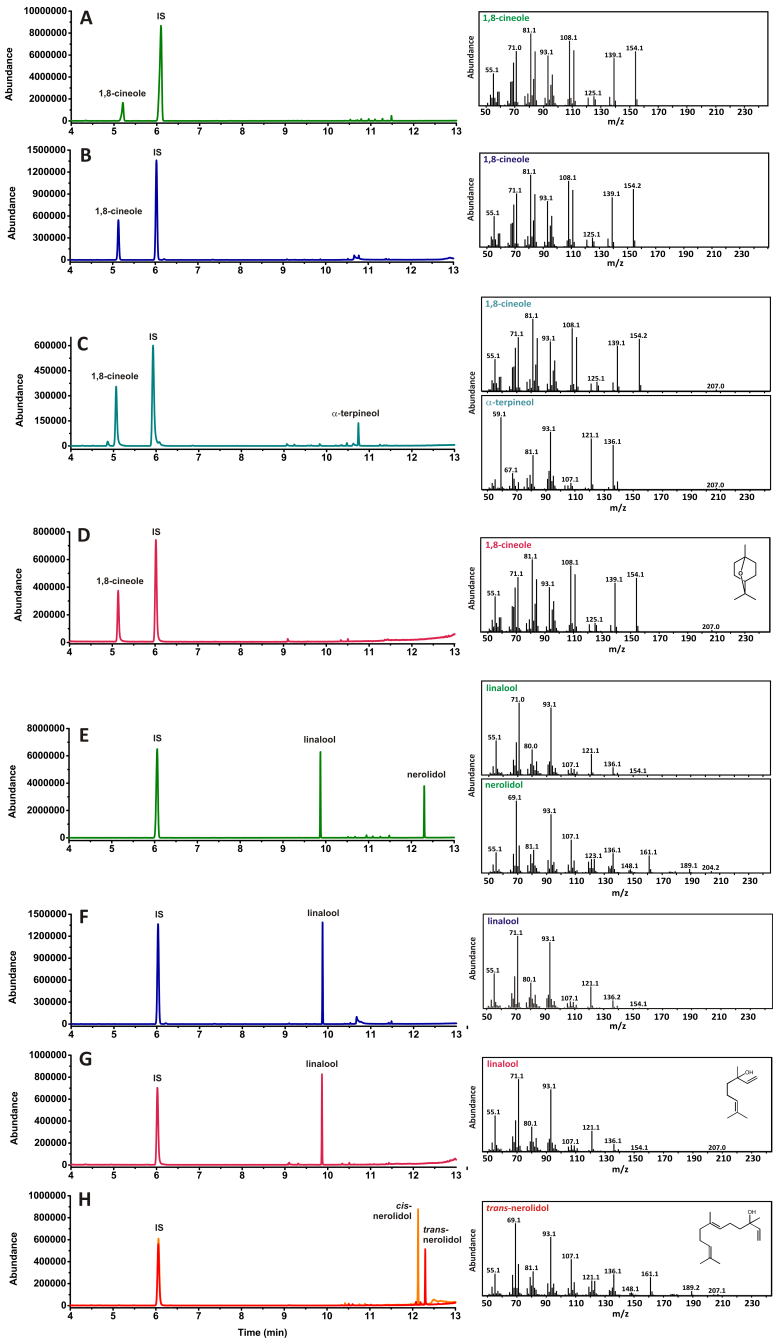

Figure 1. GC-MS analysis of bCinS and bLinS. A) bCinS product profile when inserted in an engineered *E. coli* strain capable of overproducing GPP. B) bCinS conversion of GPP (2 mM) *in vitro*. C) bCinS conversion of NPP (2 mM) *in vitro*. D) 1,8-cineole standard (0.1 mg/ml). E) bLinS product profile when inserted in an engineered *E. coli* strain capable of overproducing GPP. F) bLinS conversion of GPP

(2 mM) *in vitro*. G) *R-(–)*-linalool standard (0.1 mg/ml). H) *cis*- and *trans*-nerolidol standards (0.1 mg/ml). IS = internal standard (*sec*-butyl benzene).

Structure of the bCinS FNPP Complex

Crystals of bCinS were obtained when co-crystallised with 2-fluoro neryl pyrophosphate (FNPP), a fluorinated GPP isomer. Unfortunately, bCinS crystallised poorly when not bound to a substrate analogue. This suggests a conformational change occurs between an open (*apo*)-form and a closed (substrate-inhibitor bound) complex similar to that seen with other terpene cyclases[45, 58]. Previous studies have indicated that some terpene cyclases/synthases can also accept neryl pyrophosphate (NPP) as substrate[16]. In the case of bCinS, incubation with NPP also leads to 1,8 cineole (**Figure 1**). As observed with other terpene synthases, fluorination of the substrate blocks the key ionisation step, blocking diphosphate release and formation of the geranyl/neryl cation[28]. The bCinS-FNPP structure was determined to 1.63 Å and reveals the enzyme is a dimer of a typical class I terpenoid α-helical domain, with the active sites oriented in an anti-parallel fashion (**Figure 2a**). Analysis of the bCinS dimer revealed a total buried surface area of 4114Å^2, indicating the oligomeric state is biologically relevant (using PISA[59]). Both monomers are similar in structure (r.m.s.d. of 0.25 Å over 315 Cα atoms), with residues that constitute one of the loops close to the active site disordered. The bound FNPP is clearly defined in the electron density of both active sites, with no significant differences in conformation between both monomers (**Figure 2b**). The pyrophosphate moiety of FNPP makes extensive interactions with residues in the active site, in addition to coordination by two Mg^{2+} ions and interactions with several water molecules. While one Mg^{2+} is bound by the conserved NSE motif (Mg^{2+} B), the other is bound by the aspartate rich motif (Mg^{2+}

A). No clear density could be observed that corresponds to the location of the third metal ion (Mg^{2+} C).

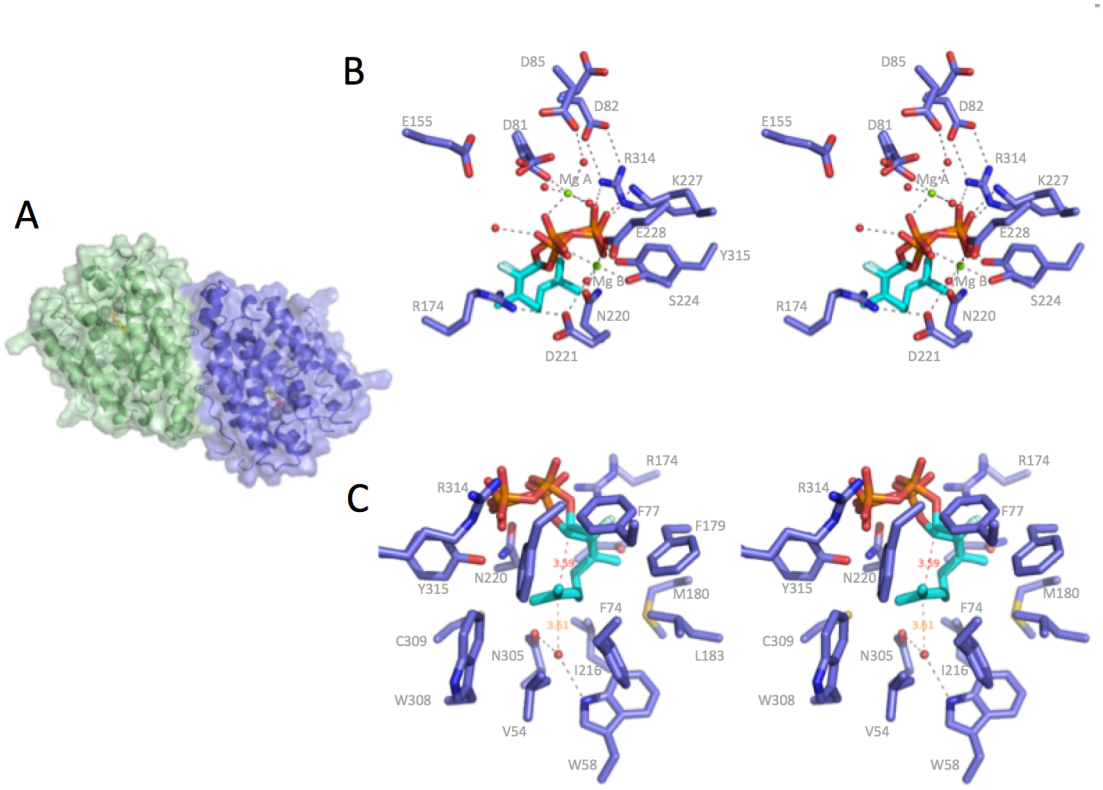

Figure 2. Structure of bCinS in complex with FNPP. A) Cartoon representation of the bCinS dimer with the solvent accessible surface shown colour coded per monomer. B) Stereoview of the FNPP-Mg^{2+} ion binding site. Key polar interactions are shown by dotted lines. The electron density indicates multiple positions of the diphosphate moiety as well as several Mg^{2+} binding residues. C) Stereoview of the FNPP hydrophobic binding pocket. A single water molecule is present, located close to the C6 atom.

EPR Reveals Binding of 3 Mn^{2+} Ions to bCinS

To ascertain whether bCinS binds to two or three Mg^{2+} ions, we employed EPR spectroscopy by titrating bCinS purified in the absence of $MgCl_2$ with Mn^{2+}. The Mn^{2+}

ion serves as a valuable probe of the Mg^{2+} ion binding sites[60-62]. This substitution allowed application of cw-EPR spectroscopy to investigate the number of potential metal binding sites in bCinS. Comparison of the EPR spectra of the aqueous $MnCl_2$ and bCinS with and without the inhibitor FGPP indicates that the spectrum of the 1:1 bCinS-FGPP:Mn^{2+} sample contains a highly resolved multiplet structure (**Figure 3a**; red spectrum). This multiplet structure is the ^{55}Mn hyperfine coupling which is due to the interaction of electron spin (S=5/2) of the Mn^{2+} ion with the nuclear spin (I = 5/2) of ^{55}Mn nucleus. It is a characteristic signature of binding of FGPP to Mn^{2+} ion, which is centered at g ~ 2.0. This multiplet feature increases in intensity only until the ratio of Mn^{2+} ion concentration relative to bCinS-FGPP reaches 3. However, where the relative concentration of Mn^{2+} ion is greater than 3, the EPR spectra show overall increase in intensity due to the contribution from free/unbound Mn^{2+} ion. The EPR spectrum of the 1:6 bCinS-FGPP:Mn^{2+} sample (**Figure 3a**; magenta spectrum) can be simulated (Fig 3a; cyan spectrum) by 1:1 addition of the EPR spectra of 1:3 bCinS-FGPP:Mn^{2+} sample with (**Figure 3a**; blue spectrum) the 1:3 bCinS:Mn^{2+} (**Figure 3a**; black spectrum). This indicates that there are 3 potential metal binding sites available in bCinS. Detailed analysis and assignment of the various transitions in the EPR spectra (**Figures S6a-b and S7a-b**) are provided in the supplementary information.

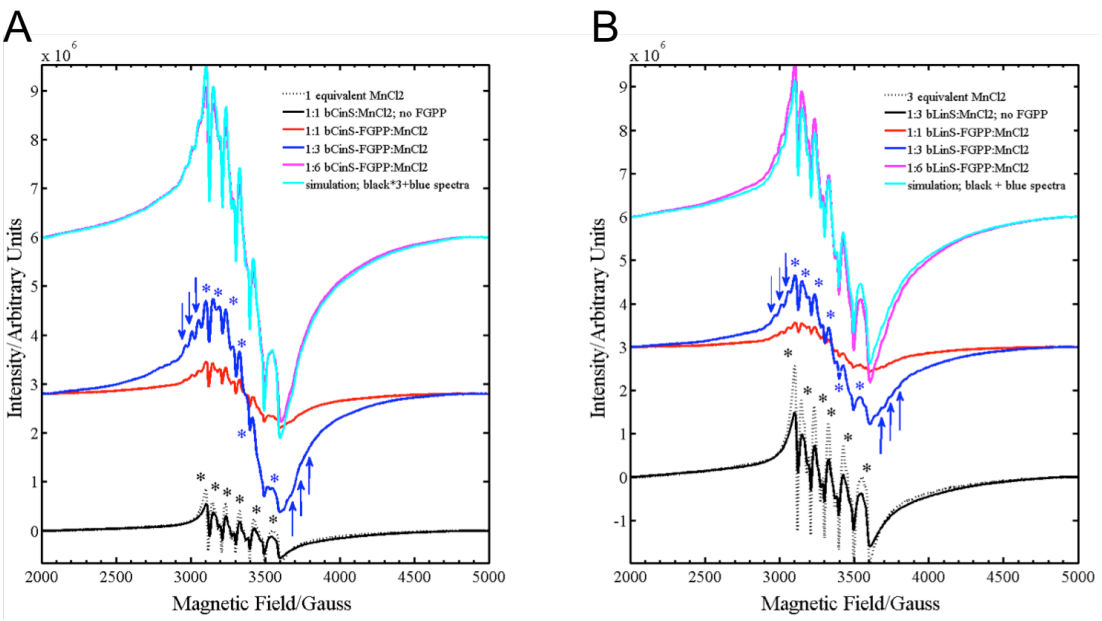

Figure 3. EPR confirms binding of 3 Mn^{2+} in solution. cw-EPR spectra of 'Mn^{2+}' substituted bCinS (A) and bLinS (B) protein samples with varying equivalents of Mn^{2+} concentration with or without FGPP measured as a frozen solution along with standard $MnCl_2$. The plot shows the multiplet EPR signal arise from the Mn^{2+} ion around the g = 2 region (from 250-400 mT).

Structure of the bCinS-FGPP Complex and bCinS Mechanism

Soaking of the bCinS-FNPP crystals with FGPP led to the partial exchange of the inhibitor in both monomers (structure determined to 1.51 Å resolution). Besides the obvious reorientation of the carbon skeleton, the presence of FGPP does not lead to active site reconfiguration. However, the soaking protocol used has led to clear electron density of a partially occupied third Mg^{2+} ion (Mg^{2+}C; **Figure 4**). This in turn is accompanied by a modest change in conformation of the E155 region (**Figure 4a**), bringing the E155 side chain into close contact with water molecules ligating Mg^{2+}C. Given the partial occupancy of the inhibitors and of the E155/Mg^{2+}C, it is unclear

whether there is a direct link between the nature of the ligand bound in the active site and the binding of Mg^{2+} C. However, as both GPP and NPP act as substrates for bCinS, presumably both requiring binding of 3 Mg^{2+} ions, it seems plausible the soaking procedure used is responsible for the observed changes in the E155 region and the associated Mg^{2+} C binding.

Based on the bCinS-FNPP and bCinsS-FGPP/FNPP structures, a mechanism for the bacterial 1,8-cineole synthesis can be proposed, by analogy to observations made with plant monoterpene synthases[18] (**Figure 5**). Unlike FGPP, the carbon chain conformation of FNPP (and by extension the NPP substrate) is compatible with cyclisation of the initial carbocation (in this case linalyl) derived from substrate ionisation to form the (*R*)-terpinyl cation. Indeed, the FNPP C1 and C6 atoms are placed at a distance of ~3.6 Å. In contrast, steric constraints require the FGPP carbon skeleton to undergo an isomerisation step following substrate ionisation and geranyl carbocation formation prior to cyclisation. For other monoterpene cyclase enzymes, this has been proposed to occur via transient formation of linalyldiphosphate and concomitant change from the transoid to cisoid configuration[14-15]. A second substrate ionisation step then generates the linalyl carbocation species, which can proceed to the cyclisation step. The fact that both GPP and NPP result in the same product suggests the exact configuration of the respective linalyl carbocation species (GPP versus NPP derived) and resulting terpinyl carbocation are similar, resembling the carbon chain configuration of the FNPP inhibitor. However, recent solution studies using labeled GPP have suggested bCinS proceeds via the (*S*)-terpinyl cation, in contrast to the (*R*)-terpinyl configuration proposed on the basis of the bCinS-FNPP crystal structure[63]. Following formation of the terpinyl carbocation, conversion via the

final cyclisation step to the 1,8-cineol product is proposed to occur via a *syn* addition[63]. With the exception of a single water molecule, coordinated by Trp58 and Asn305, the hydrophobic binding pocket is devoid of solvent. This water molecule is placed at a distance of ~3.6 Å to the C6 of FNPP (**Figure 2c**), and thus appears the most likely candidate for nucleophilic attack on the terpinyl cation. MD simulations show that this water molecule remains at an average distance of 3.84 (±0.45 run1, (±0.53 run2) Å from C7 of GPP throughout the 100 ns simulation (**Figure 6**). The water molecule interacts with Asn305, but no longer interacts with Trp58. Figure 6 (A-C) shows the different positions of the hydrocarbon tail of GPP and NPP in the representative structure from the dominant cluster for the 100 ns simulations. The hydrocarbon tail of NPP occupies the position adopted by the sidechain of Phe77 in the simulations of bCinS with GPP. There are more water molecules near to C7 of NPP and the shortest distance is not with a single water molecule throughout the entire simulation, as was observed for GPP. However, simulations with NPP show that the average position of the water molecule is more distant than in the bCinS/GPP system with an average C7 – WAT O distance of 4.26 ±0.59 Å run1 and 4.42±0.59 Å in run1 (**Figure 6 (d-e)**). Formation of the neutral α-terpineol through deprotonation is avoided by the lack of any suitable acid-base group in close proximity of this water molecule. Production of the bicyclic 1,8-cineole from the protonated α-terpineol species is proposed to occur via intramolecular proton transfer to C2, followed by C2-O bond formation leading to formation of the second cycle. Considering the relative position of the water molecule and the C2 atom in the FNPP structure, this scenario will require some conformational changes to occur. This is distinct from the proposed mechanism for the plant 1,8 cineole synthase, for which a *syn* addition of water is

proposed, requiring no significant conformational changes prior the ensuing heterocyclization step[64].

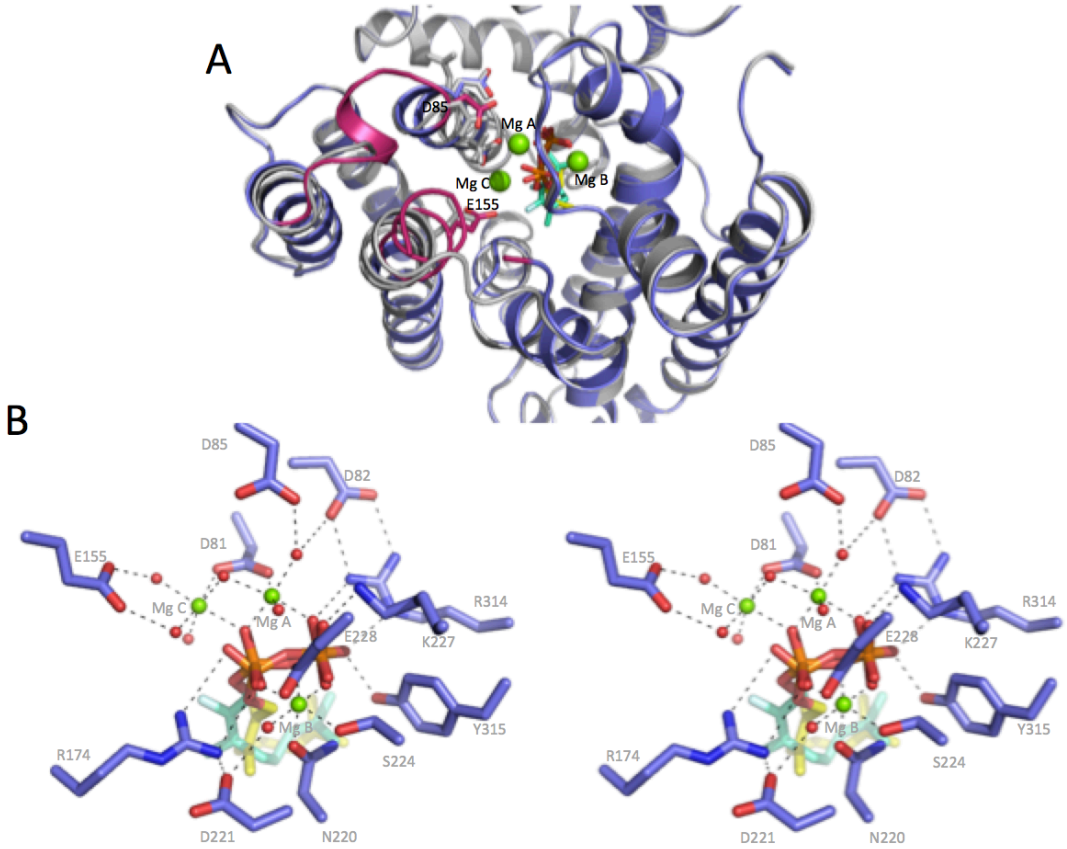

Figure 4. Structure of bCinS in complex with FGPP. A) Cartoon representation of an overlay of the bCinS-FNPP complex structure (in grey) with the bCinS-FGPP/FNPP structure obtained by soaking bCinS-FNPP with GFPP (in blue). A loop region C-terminal to D85 as well as the region surrounding E155 adopt distinct conformations in response to binding of Mg^{2+} C, these regions are coloured in red. B) Stereoview of the FGPP/FNPP-Mg^{2+} ion binding site. Key polar interactions are shown by dotted lines.

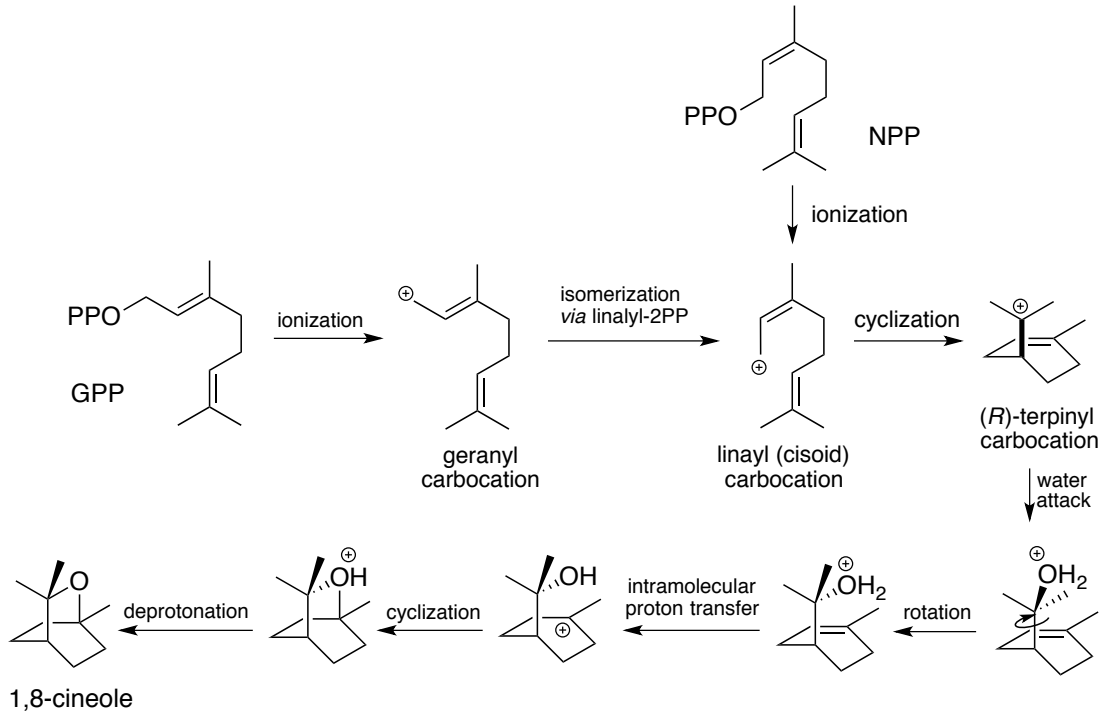

Figure 5. Mechanistic proposal for bCinS. A schematic outline of a putative mechanism for the conversion of GPP and NPP to the 1,8 cineole product by bCinS. Taking into account the observed position and orientation of the bCinS ligands and adjacent water molecules, we propose that the (*R*)-terpinyl carbocation intermediate is formed, followed by the *anti*-addition of water, requiring a rotation step prior to hetercyclization.

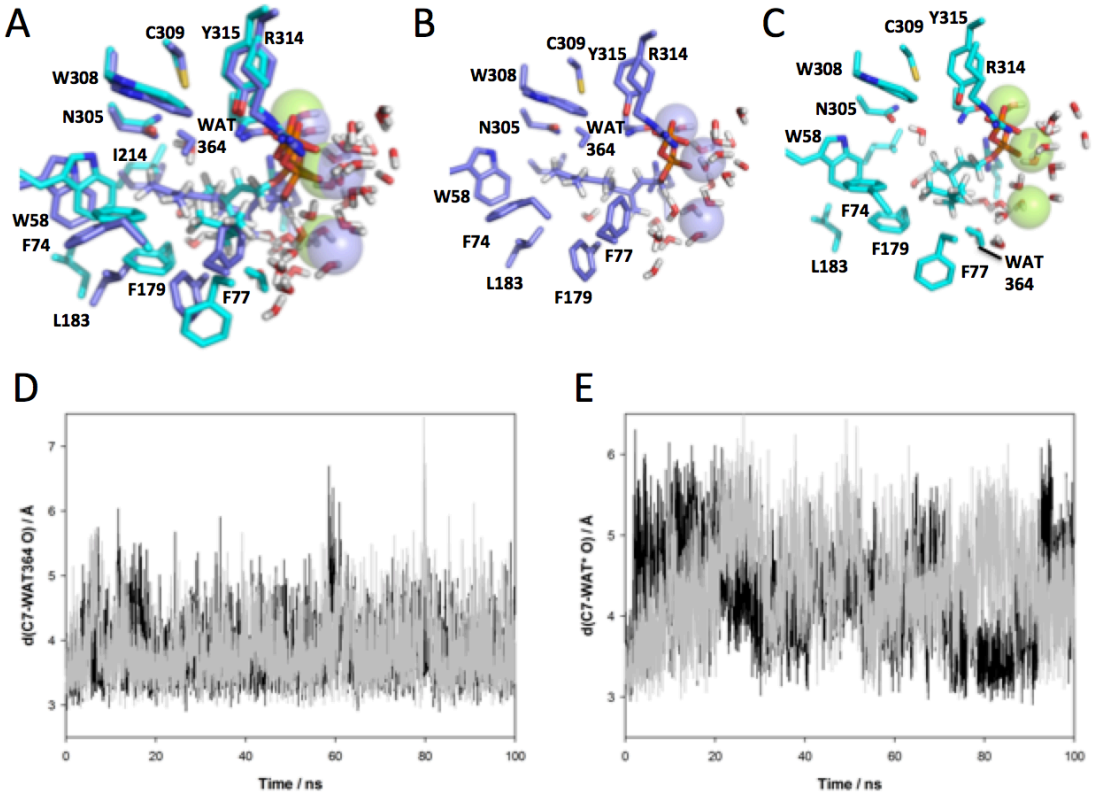

Figure 6. MD of bCinS with 3 Mg^{2+} ions and GPP or NPP. A) Active site of bCinS in the dominant cluster from MD simulations with of bCinS/GPP (purple) and bCinS/NPP (cyan). Water molecules within 5 Å of GPP are shown in stick form and the closest water molecule to C7, the site of attack by the water molecule, is coloured in purple for bCinS/GPP and cyan for bCinS/NPP. B) and C) show the same view of bCinS/GPP and bCinS/NPP alone, respectively. D) The distance between C7 and O of WAT364 over the course of 2 100 ns MD simulations of bCinS/GPP. E) The distance between C7 and O of the closest water molecule to C7 of NPP over the course of 2 100 ns MD simulations.

Structures of *Apo*-bLinS and bLinS-FGPP Complex

The bLinS could be crystallised in both the *apo* form (2.4 Å) as well as in complex with the substrate analogue FGPP (1.82 Å, **Table 1**). The bLinS structure reveals a

dimer in the asymmetric unit, but the monomer interface is distinct to that observed for the bCinS enzyme (**Figure 7a**). The individual bLinS monomers overlay with r.m.s.d of 0.83Å for 293 Cα atoms, with a small shift in position of the N-terminal region encompassing the first two alpha helices (residues 1-62) located furthest away from the dimer interface. Co-crystallisation with FGPP leads to crystals with similar packing. Unexpectedly, clear electron density corresponding to FGPP is only present in monomer A (**Figure 7b**). In contrast, electron density occupying the active site of monomer B is weak, and only a single phosphate ion could be modelled that might be associated with a disordered binding of the FGPP diphosphate moiety (**Figure 7c**).

The FGPP is bound to the bLinS active site of chain A in an extended conformation compared to the FGPP/FNPP configuration observed in the bCinS structures (**Figure 7d**). Only one Mg^{2+} ion coordinating the pyrophosphate moiety could be unambiguously modelled. This Mg^{2+} ion sits on the concave side of the PP_i moiety and hydrogen bonds with Asp80 of the aspartate-rich motif in helix D. The direct interactions between the diphosphate moiety of FGPP and bLinS are limited to a polar interaction with Lys225. The hydrophobic moiety of FGPP is located in a predominantly hydrophobic pocket at the core of the bLinS structure, with a polar interaction observed between Asn218 of the Mg^{2+} B binding NSE motif and the FGPP fluorine atom. The lack of Mg^{2+} binding to the NSE motif, and the unusual position of the diphosphate moiety, suggests the FGPP is bound in a non-catalytic mode. We again used EPR to establish bLinS binds to three Mn^{2+} ions (and by extension 3 Mg^{2+}) in solution, similar to other terpene synthases (**Figure 3b**). While the electron density in the active site of bLinS monomer B corresponds to a disordered species, the position of the single phosphate that is visible is more akin to what can be expected

for the catalytic binding mode when superimposing bLinS on the bCinS ligand complex structures (**Figure 7e**). The phosphate in the bLinS monomer B establishes a network of polar contacts with the C-terminal region (R308, Y309) that is disordered in the *apo*-bLinS structure. It is furthermore positioned adjacent to the NSE motif, although a Mg^{2+} B ion could not be unambiguously located in this area. The ordering of the C-terminal region is incompatible with crystal packing for bLinS monomer A, possibly contributing to the non-catalytic conformation observed for the bound FGPP in the corresponding active site. A comparison with the *apo*-bLinS structure reveals the overall conformation for both monomers is similar, with the notable exception of the C-terminal region. However, class I terpenoid synthase structures have been found to alternate between an 'open' state (i.e. *apo*) and a 'closed' (i.e. ligand) bound state[58–65]. This calls into question whether the *apo*-bLinS structure is reflective of the open state, or whether the bLinS-FGPP complex corresponds to the closed state. The fact neither of the monomers in the bLinS-FGPP complex binds to the required three metal ions strongly suggests both *apo* bLinS and the bLinS-FGPP structures are in the open state, possibly stabilised by crystal packing contacts.

MD simulations suggest that, unlike other terpene synthases, neither bLinS or bCinS undergo a major conformational changes to between 'open' and closed states, (**Figures S8a-c** and **S9a-c**). Although bLinS-FGPP is likely to correspond to the open state, the carbon chain of the bound FGPP (in monomer A) occupies a similar region as observed in the bCinS-FGPP/FNPP complexes (**Figure 7e**). This likely indicates the position of the active site hydrophobic pocket in bLinS, and might even reflect the corresponding conformation of carbon chain of the bound FGPP in the closed state. As linalool is an acyclic monoterpene product, the bLinS catalytic mechanism does

not require a cyclisation process. Instead, the geranyl cation attacks a nearby water molecule leading to linalool following deprotonation (**Figure 8a**). In the bLinS-FNPP structure, several water molecules are located within a distance of ~4.5Å from the FGPP (**Figure 7d**), and representing likely candidates for this process in case the FGPP carbon chain conformation is reflective of the catalytically relevant species. In contrast to the closed nature of the bCinS structure, the bLinS is relatively open, and we cannot rule out further closure might occur upon substrate binding in solution. Keeping this caveat in mind, the most likely candidate for the water attack is the molecule that is coordinated by Asp79 and Arg172 and is at a distance of 3.6Å from C3 of FGPP. The position of the water molecule with respect to FGPP suggests production of *R*-(–)-linalool, which matches with the biochemical characterisation. MD simulations show that the closest water molecule to C3 of GPP remains at an average distance of 3.29 (±0.21) Å in run1 and 3.93 (±0.52) Å in run2 (**Figure 8c**). MD simulations of bLinS in complex with FPP (**Figure S9**), the precursor to sesquiterpenes, shows that the active site is sufficiently large to accommodate a sesquiterpene, explaining the fact bLinS also accepts FPP as a substrate[23].

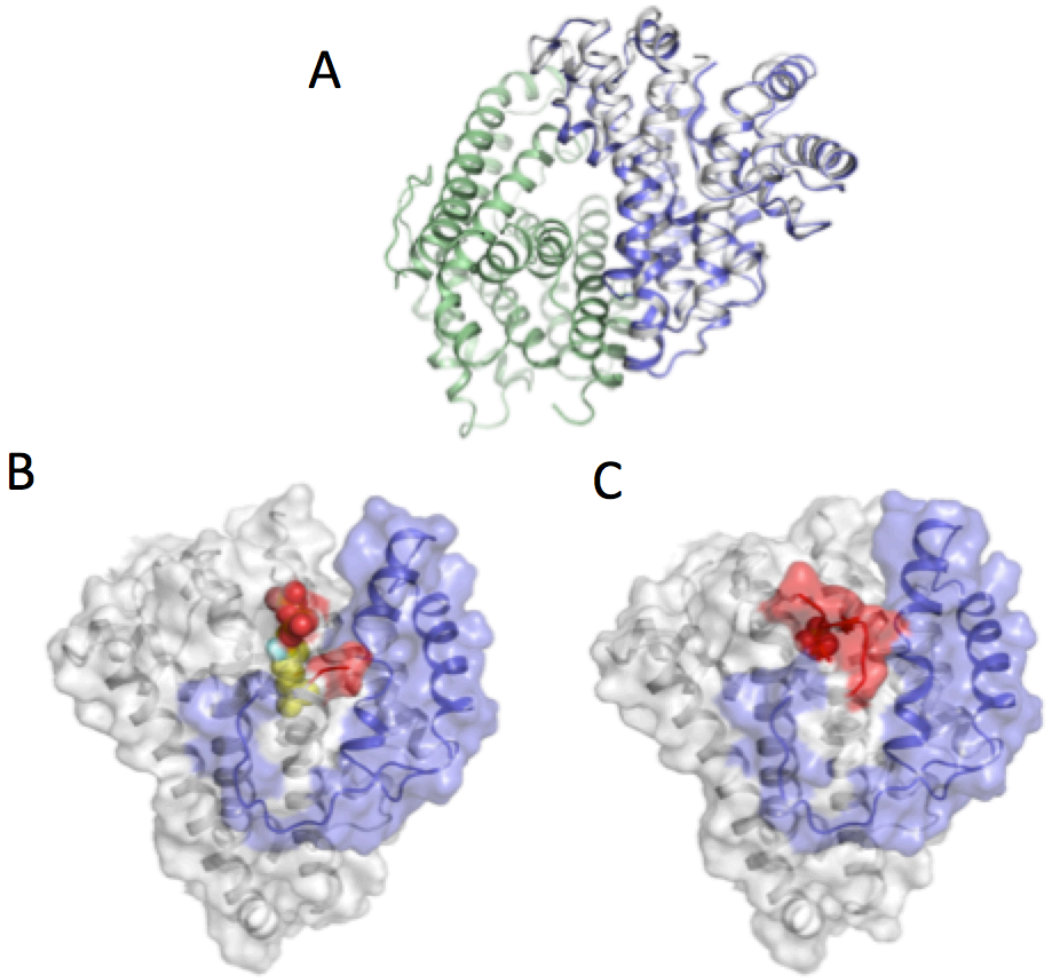
A
B
C

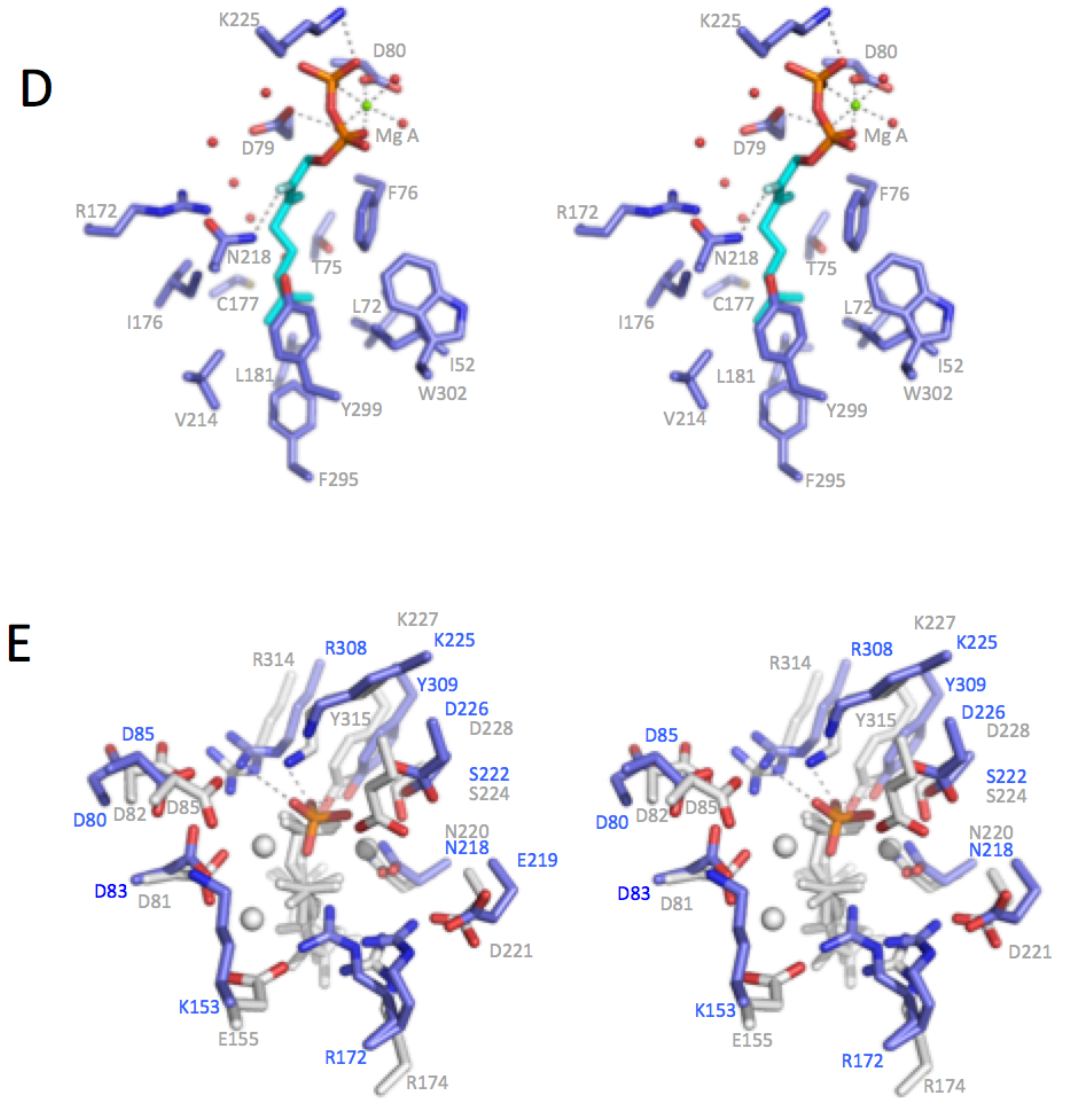

Figure 7. Structure of bLinS in *apo* and FGPP complex form. A) Cartoon representation of the *apo* bLinS dimer, with one monomer coloured in green and the second monomer in blue. The latter is overlaid with the first monomer (in grey) revealing small changes in conformation occur distant from the dimer interface. B) Cartoon representation of monomer A bound to FGPP. The N-terminal region is shown in blue and the (here disordered) C-terminal region in red. C) Cartoon representation of the monomer B bound to phosphate. Orientation and colour coding are as in panel B. The ordering of the C-terminus and the partial closing of the N-terminal regions occludes the phosphate from solvent, in contrast to the solvent exposed nature of the diphosphate group in monomer A. D) Stereoview of the active

site of bLinS monomer A in complex with FGPP. Key polar interactions are shown by black dotted lines. E) Stereoview of the active site of bLinS monomer B (in blue) in overlay with the active site of bCinS in complex with FGPP/FNPP (in grey).

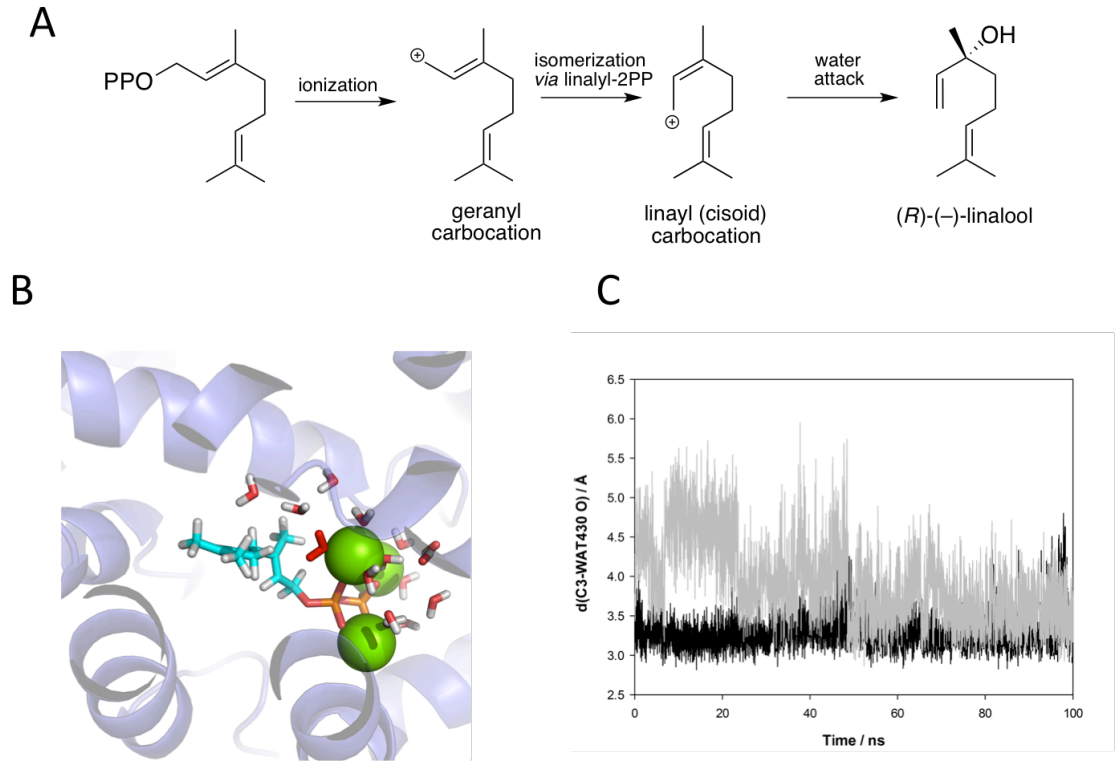

Figure 8. Mechanistic proposal for bLinS and MD of bLinS with GPP and 3 Mg^{2+} ions. A) A schematic outline representing the conversion of GPP to the linalool product by bLinS. B) Active site of bLinS in the dominant cluster from MD simulations with GPP and 3 Mg^{2+} ions. GPP is shown with cyan carbon atoms, bLinS is shown in purple in cartoon form and the Mg^{2+} ions are shown as green spheres. Water molecules within 5 Å of GPP are shown in stick form, with the water molecule closest to C3 of GPP shown in red. C) The distance between C3 and O of WAT430 over the course of 2 100 ns MD simulations.

Bacterial mTC/S are Structurally Similar to Sesquiterpene Synthases

The bLinS and bCinS are single domain (α) enzymes whereas the plant mTC(S) typically contain two domains (α and β). This makes them structurally more similar to the sesquiterpene synthases (**Figure 9a**), which are also usually composed of only a single class I terpenoid fold domain[10]. It is notable that genome mining for bacterial terpene synthase-like genes followed by heterologous expression revealed the majority of these enzymes made sesquiterpenes as products[20]. So far, bLinS and bCinS are the only characterised bacterial mTC(S) that accept GPP as substrate and thus lead to monoterpene formation. The bCinS-FNPP complex is specifically compared to the structures of plant limonene synthases[15-16] and bornyl diphosphate synthase[14] for which complexes with the substrate analogues are available. When comparing the corresponding C-terminal catalytic domains with the bCinS complexes, it is clear that the orientation of GPP/NPP analogue in bCinS is such that the beta phosphate occupies the location comparable to the alpha phosphate binding site in the plant enzymes and *vice versa*, and resembles the orientation observed in sesquiterpene synthase complex. For the functionally analogous plant 1,8-cineole synthase (Sf-CinS1) only the apo-enzyme structure is available. Furthermore, superimposition of the bCinS and Sf-CinS1 reveals distinct active site architectures. In Sf-CinS1, Asn338, which coordinates a water molecule, was found to be crucial for the synthesis of 1,8-cineole[18]. Mutation of Asn338 to Ile resulted in the formation of sabinene as the major product but no α-terpineol and 1,8-cineole, establishing the role of Asn338 in water capture. In bCinS, as mentioned before, residues Trp58 and Asn305 coordinate the water molecule proposed to be involved in the water attack. Though Asn305 in bCinS resides in a different helix and region of the active site compared to Asn338 in Sf-CinS1, Asn305 might play a similar role to as proposed for

the plant enzyme (**Figure S10**). Analysis using DALI[66] and PDBefold[67] servers showed many sesquiterpene synthases including pentalenene synthase (PDB 1ps1)[32], germacradienol synthase (PDB 5i1u)[68], hedycaryol synthase (PDB 4mc3)[69], geosmin synthase (PDB 5dz2)[70], epi-isozizaene synthase (PDB 4ltv)[65], selinadiene synthase (40kz)[58] and aristolochene synthase (PDB 4kwd)[51] are very similar to bLinS and bCinS structures (**Table S2**).

Two sesquiterpene synthase structures have been reported in complex with substrate analogues: *Aspergillus terreus* aristocholene synthase (ATAS) with farnesyl thiolodiphosphate (FSPP; PDB 4KUX) and selinadiene synthase (SdS) with dihydrofarnesyl diphosphate (DHFPP; PDB 4OKZ). A comparison of these structures with bLinS and bCinS might allow pinpointing of those active site differences that play a role in determining substrate specificity (C_{10} versus C_{15}). Since the Mg^{2+} and pyrophosphate binding regions are highly conserved, most variations in the active site architecture are restricted to hydrophobic cavity surrounding the substrate carbon chain. In bCinS, two phenylalanines (Phe 77 and Phe 179) constrict the substrate-binding site when compared to the ATAS-FSPP and SdS-DHFPP structures, and would clash with a putative FPP substrate (**Figure 9b**). Phe179 resides in the kink region of the helix G1/2 of bCinS, and is replaced by Gly174 in ATAS and Ala183 in SdS. The bCinS Phe77 resides in helix D and is homologous to Leu80 in ATAS / Leu78 in SdS, with the latter both adopting a conformation that is pointing away from the active site. This suggests bCinS evolved from a sesquiterpene synthase by restricting active site volume.

Interestingly, bLinS contains non-aromatic residues at positions equivalent to bCinS Phe77 and Phe179 (Thr75 and Cys177 in bLinS), and thus resembles ATAS and SdS (**Figure 9c**). This provides a rationale for the fact bLinS can accept both GPP and FPP as substrates but bCinS can only convert GPP[22-23].

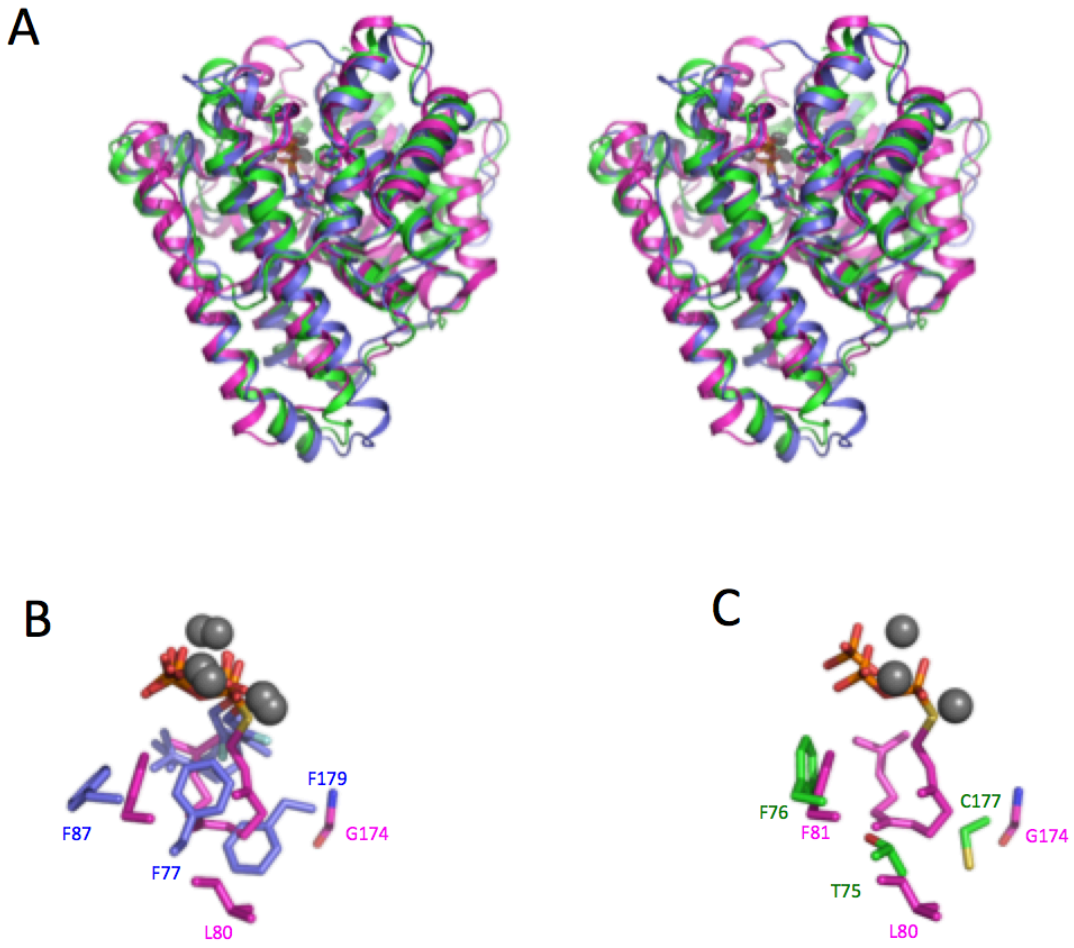

Figure 9. bLinS and bCinS are related to bacterial sesquiterpene synthases. A) Stereoview of a cartoon representation of a structural overlay of bLinS (monomer B; in green), bCinS FGPP/FNPP (in blue) and aristolochene synthase (ATAS) (PDB code 4KUX) in complex with a C15 substrate analogue (in magenta). B) Active site overlay of bCinS and ATAS, colour coding as in panel A. C) Active site overlay of bLinS (monomer B) and ATAS, colour coding as in panel A.

CONCLUSIONS

We have shown that expression of *Streptomyces clavuligerus* linalool synthase and 1,8-cineole synthase in an *E. coli* geranyl diphosphate producing strain leads to higher levels of production (linalool) or more enriched product profiles (1,8-cineole) than previously reported. Crystal structures of both *S. clavuligerus* monoterpene synthases reveal the bacterial monoterpene synthases are more similar to previously characterised sesquiterpene synthases. A comparison with the sesquiterpene synthases allowed identification of key residues that can be exploited for rational design and switching of activity between the two classes. These results provide a basis for application of the bacterial monoterpene synthases to generate diverse monoterpene scaffolds and employ synthetic biology approaches for large-scale monoterpenoid production.

ASSOCIATED CONTENT

Supporting Information

Extended EPR results and discussion, Scheme S1, Figures S1-S10, Tables S1-S2.

AUTHOR INFORMATION

Corresponding Author

*N.S.S.: e-mail, nigel.scrutton@manchester.ac.uk; tel, +44 161 306 5152.

Author Contributions

V.K. expressed, purified and crystallised proteins, collected X-ray data and solved the structures. N.G.H.L. carried out the monoterpenoids production experiments in *E. coli*. K.E.R. and L.O.J. carried out the simulation experiments with guidance from

M.W.v.d.K., S.H. and A.J.M. A.N.C synthesised GPP and NPP analogues with support from J.M.G. M.S. performed EPR experiments with help from S.H. N.J.B. and L.J.K. helped with optimizing protein purification. V.K. and D.L. analysed the crystal structures. N.S.S., D.L., A.J.M. and E.T. initiated the project. V.K., K.E.R., D.L. and N.S.S. wrote the manuscript with inputs from all authors.

Notes

The authors declare no competing financial interests.

ACKNOWLEDGEMENTS

We thank Colin Levy, Manchester Protein Structure Facility (MPSF) for help with X-ray data collection, Matthew J. Cliff for NMR analysis of synthetic compounds and Derren J. Heyes for project management. We thank Diamond Light Source for access to beamlines I04 and I04-1 (proposal number mx12788). This work was funded by the UK Biotechnology and Biological Sciences Research Council (BBSRC; BB/M000354/1, BB/M017702/1 and BB/L027593/1:ERA-IB2 TERPENOSOME). D.L. is a Royal Society Wolfson Merit Award holder. M.W.v.d.K. is a BBSRC David Phillips Fellow. N.S.S. was a Royal Society Wolfson Merit Award holder and is an Engineering and Physical Sciences Research Council (EPSRC; EP/J020192/1) Established Career Fellow.

ABBREVIATIONS

bLinS, linalool/nerolidol synthase; bCinS, 1,8-cineole synthase; GPP, geranyl pyrophosphate; NPP, neryl pyrophosphate; FGPP, 2-fluoro geranyl pyrophosphate; FNPP, 2-fluoro neryl pyrophosphate; FPP, farnesyl pyrophosphate

REFERENCES

1. Tholl, D. *Adv Biochem Eng Biotechnol* **2015,** 148, 63-106.
2. George, K. W.; Alonso-Gutierrez, J.; Keasling, J. D.; Lee, T. S. *Adv Biochem Eng Biotechnol* **2015,** 148, 355-89.
3. Leferink, N. G. H.; Jervis, A. J.; Zebec, Z.; Toogood, H. S.; Hay, S.; Takano, E.; Scrutton, N. S. *Chemistryselect* **2016,** 1, 1893-1896.
4. Peralta-Yahya, P. P.; Zhang, F.; del Cardayre, S. B.; Keasling, J. D. *Nature* **2012,** 488, 320-8.
5. Jongedijk, E.; Cankar, K.; Buchhaupt, M.; Schrader, J.; Bouwmeester, H.; Beekwilder, J. *Appl Microbiol Biotechnol* **2016,** 100, 2927-38.
6. Zebec, Z.; Wilkes, J.; Jervis, A. J.; Scrutton, N. S.; Takano, E.; Breitling, R. *Curr Opin Chem Biol* **2016,** 34, 37-43.
7. Wang, X.; Ort, D. R.; Yuan, J. S. *Plant Biotechnol J* **2015,** 13, 137-46.
8. Formighieri, C.; Melis, A. *Photosynth Res* **2016,** 130, 123-135.
9. Oldfield, E.; Lin, F. Y. *Angew Chem Int Ed Engl* **2012,** 51, 1124-37.
10. Gao, Y.; Honzatko, R. B.; Peters, R. J. *Nat Prod Rep* **2012,** 29, 1153-75.
11. Aaron, J. A.; Christianson, D. W. *Pure Appl Chem* **2010,** 82, 1585-1597.
12. Srividya, N.; Davis, E. M.; Croteau, R. B.; Lange, B. M. *Proc Natl Acad Sci U S A* **2015,** 112, 3332-7.
13. Hyatt, D. C.; Croteau, R. *Arch Biochem Biophys* **2005,** 439, 222-33.
14. Whittington, D. A.; Wise, M. L.; Urbansky, M.; Coates, R. M.; Croteau, R. B.; Christianson, D. W. *Proc Natl Acad Sci U S A* **2002,** 99, 15375-80.
15. Hyatt, D. C.; Youn, B.; Zhao, Y.; Santhamma, B.; Coates, R. M.; Croteau, R. B.; Kang, C. *Proc Natl Acad Sci U S A* **2007,** 104, 5360-5.
16. Kumar, R. P.; Morehouse, B. R.; Matos, J. O.; Malik, K.; Lin, H.; Krauss, I. J.; Oprian, D. D. *Biochemistry* **2017,** 56, 1716-1725.
17. Morehouse, B. R.; Kumar, R. P.; Matos, J. O.; Olsen, S. N.; Entova, S.; Oprian, D. D. *Biochemistry* **2017,** 56, 1706-1715.
18. Kampranis, S. C.; Ioannidis, D.; Purvis, A.; Mahrez, W.; Ninga, E.; Katerelos, N. A.; Anssour, S.; Dunwell, J. M.; Degenhardt, J.; Makris, A. M.; Goodenough, P. W.; Johnson, C. B. *Plant Cell* **2007,** 19, 1994-2005.
19. Rudolph, K.; Parthier, C.; Egerer-Sieber, C.; Geiger, D.; Muller, Y. A.; Kreis, W.; Muller-Uri, F. *Acta Crystallogr F Struct Biol Commun* **2016,** 72, 16-23.
20. Yamada, Y.; Kuzuyama, T.; Komatsu, M.; Shin-Ya, K.; Omura, S.; Cane, D. E.; Ikeda, H. *Proc Natl Acad Sci U S A* **2015,** 112, 857-62.
21. Yamada, Y.; Arima, S.; Nagamitsu, T.; Johmoto, K.; Uekusa, H.; Eguchi, T.; Shin-ya, K.; Cane, D. E.; Ikeda, H. *J Antibiot (Tokyo)* **2015,** 68, 385-94.
22. Nakano, C.; Kim, H. K.; Ohnishi, Y. *Chembiochem* **2011,** 12, 1988-91.
23. Nakano, C.; Kim, H. K.; Ohnishi, Y. *Chembiochem* **2011,** 12, 2403-7.
24. Dickschat, J. S. *Nat Prod Rep* **2016,** 33, 87-110.
25. Koksal, M.; Chou, W. K.; Cane, D. E.; Christianson, D. W. *Biochemistry* **2012,** 51, 3011-20.
26. Lapczynski, A.; Letizia, C. S.; Api, A. M. *Food Chem Toxicol* **2008,** 46, S190-2.
27. Seol, G. H.; Kim, K. Y. *Adv Exp Med Biol* **2016,** 929, 389-398.

28. Karp, F.; Zhao, Y.; Santhamma, B.; Assink, B.; Coates, R. M.; Croteau, R. B. *Arch Biochem Biophys* **2007,** 468, 140-6.
29. Dixit, V. M.; Laskovics, F. M.; Noall, W. I.; Poulter, C. D. *J Org Chem* **1981,** 46, 1967-1969.
30. Winter, G.; Lobley, C. M.; Prince, S. M. *Acta Crystallogr D Biol Crystallogr* **2013,** 69, 1260-73.
31. Kabsch, W. *Acta Crystallogr D Biol Crystallogr* **2010,** 66, 125-32.
32. Lesburg, C. A.; Zhai, G.; Cane, D. E.; Christianson, D. W. *Science* **1997,** 277, 1820-4.
33. McCoy, A. J.; Grosse-Kunstleve, R. W.; Adams, P. D.; Winn, M. D.; Storoni, L. C.; Read, R. J. *J Appl Crystallogr* **2007,** 40, 658-674.
34. Adams, P. D.; Afonine, P. V.; Bunkoczi, G.; Chen, V. B.; Davis, I. W.; Echols, N.; Headd, J. J.; Hung, L. W.; Kapral, G. J.; Grosse-Kunstleve, R. W.; McCoy, A. J.; Moriarty, N. W.; Oeffner, R.; Read, R. J.; Richardson, D. C.; Richardson, J. S.; Terwilliger, T. C.; Zwart, P. H. *Acta Crystallogr D Biol Crystallogr* **2010,** 66, 213-21.
35. Emsley, P.; Lohkamp, B.; Scott, W. G.; Cowtan, K. *Acta Crystallogr D* **2010,** 66, 486-501.
36. Afonine, P. V.; Grosse-Kunstleve, R. W.; Echols, N.; Headd, J. J.; Moriarty, N. W.; Mustyakimov, M.; Terwilliger, T. C.; Urzhumtsev, A.; Zwart, P. H.; Adams, P. D. *Acta Crystallogr D Biol Crystallogr* **2012,** 68, 352-67.
37. Joosten, R. P.; Long, F.; Murshudov, G. N.; Perrakis, A. *IUCrJ* **2014,** 1, 213-20.
38. Chen, V. B.; Arendall, W. B., 3rd; Headd, J. J.; Keedy, D. A.; Immormino, R. M.; Kapral, G. J.; Murray, L. W.; Richardson, J. S.; Richardson, D. C. *Acta Crystallogr D Biol Crystallogr* **2010,** 66, 12-21.
39. MacKerell, A. D.; Bashford, D.; Bellott, M.; Dunbrack, R. L.; Evanseck, J. D.; Field, M. J.; Fischer, S.; Gao, J.; Guo, H.; Ha, S.; Joseph-McCarthy, D.; Kuchnir, L.; Kuczera, K.; Lau, F. T. K.; Mattos, C.; Michnick, S.; Ngo, T.; Nguyen, D. T.; Prodhom, B.; Reiher, W. E.; Roux, B.; Schlenkrich, M.; Smith, J. C.; Stote, R.; Straub, J.; Watanabe, M.; Wiorkiewicz-Kuczera, J.; Yin, D.; Karplus, M. *Journal of Physical Chemistry B* **1998,** 102, 3586-3616.
40. Foloppe, N.; MacKerell, A. D. *J Comput Chem* **2000,** 21, 86-104.
41. Olsson, M. H. M.; Sondergaard, C. R.; Rostkowski, M.; Jensen, J. H. *J Chem Theory Comput* **2011,** 7, 525-537.
42. Sondergaard, C. R.; Olsson, M. H. M.; Rostkowski, M.; Jensen, J. H. *J Chem Theory Comput* **2011,** 7, 2284-2295.
43. Jorgensen, W. L.; Chandrasekhar, J.; Madura, J. D.; Impey, R. W.; Klein, M. L. *J Chem Phys* **1983,** 79, 926-935.
44. Humphrey, W.; Dalke, A.; Schulten, K. *J Mol Graph Model* **1996,** 14, 33-38.
45. van der Kamp, M. W.; Sirirak, J.; Zurek, J.; Allemann, R. K.; Mulholland, A. J. *Biochemistry* **2013,** 52, 8094-105.
46. Major, D. T.; Freud, Y.; Weitman, M. *Curr Opin Chem Biol* **2014,** 21, 25-33.
47. O'Brien, T. E.; Bertolani, S. J.; Tantillo, D. J.; Siegel, J. B. *Chem Sci* **2016,** 7, 4009-4015.
48. Allner, O.; Nilsson, L.; Villa, A. *J Chem Theory Comput* **2012,** 8, 1493-1502.
49. Götz, A. W.; Williamson, M. J.; Xu, D.; Poole, D.; Le Grand, S.; Walker, R. C. *Journal of Chemical Theory and Computation* **2012,** 8, 1542-1555.

50. Case, D. A.; Betz, R. M.; Cerutti, D. S.; Cheatham, T. E., III ; Darden, T. A.; Duke, R. E.; Giese, T. J.; Gohlke, H.; Goetz, A. W.; Homeyer, N.; Izadi, S.; Janowski, P.; Kaus, J.; Kovalenko, A.; Lee, T. S.; LeGrand, S.; Li, P.; Lin, C.; Luchko, T.; Luo, R.; Madej, B.; Mermelstein, D.; Merz, K. M.; Monard, G.; Nguyen, H.; Nguyen, H. T.; Omelyan, I.; Onufriev, A.; Roe, D. R.; Roitberg, A.; Sagui, C.; Simmerling, C. L.; Botello-Smith, W. M.; Swails, J.; Walker, R. C.; Wang, J.; Wolf, R. M.; Wu, X.; Xiao, L.; Kollman, P. A. AMBER 2016, University of California, San Francisco.
51. Chen, M.; Al-lami, N.; Janvier, M.; D'Antonio, E. L.; Faraldos, J. A.; Cane, D. E.; Allemann, R. K.; Christianson, D. W. *Biochemistry* **2013,** 52, 5441-53.
52. Aaron, J. A.; Lin, X.; Cane, D. E.; Christianson, D. W. *Biochemistry* **2010,** 49, 1787-1797.
53. Alonso-Gutierrez, J.; Chan, R.; Batth, T. S.; Adams, P. D.; Keasling, J. D.; Petzold, C. J.; Lee, T. S. *Metab Eng* **2013,** 19, 33-41.
54. Fujisaki, S.; Nishino, T.; Katsuki, H. *J Biochem* **1986,** 99, 1327-37.
55. Zhou, J.; Wang, C.; Yoon, S. H.; Jang, H. J.; Choi, E. S.; Kim, S. W. *J Biotechnol* **2014,** 169, 42-50.
56. Liu, W.; Zhang, R.; Tian, N.; Xu, X.; Cao, Y.; Xian, M.; Liu, H. *Bioengineered* **2015,** 6, 288-93.
57. Wang, C. L.; Park, J. E.; Choi, E. S.; Kim, S. W. *Biotechnol J* **2016,** 11, 1291-1297.
58. Baer, P.; Rabe, P.; Fischer, K.; Citron, C. A.; Klapschinski, T. A.; Groll, M.; Dickschat, J. S. *Angew Chem Int Ed Engl* **2014,** 53, 7652-6.
59. Krissinel, E.; Henrick, K. *J Mol Biol* **2007,** 372, 774-97.
60. Morrissey, S. R.; Horton, T. E.; DeRose, V. J. *Journal of the American Chemical Society* **2000,** 122, 3473-3481.
61. DeRose, V. J. *Curr Opin Struct Biol* **2003,** 13, 317-24.
62. Stich, T. A.; Lahiri, S.; Yeagle, G.; Dicus, M.; Brynda, M.; Gunn, A.; Aznar, C.; Derose, V. J.; Britt, R. D. *Appl Magn Reson* **2007,** 31, 321-341.
63. Rinkel, J.; Rabe, P.; Zur Horst, L.; Dickschat, J. S. *Beilstein J Org Chem* **2016,** 12, 2317-2324.
64. Wise, M. L.; Urbansky, M.; Helms, G. L.; Coates, R. M.; Croteau, R. *J Am Chem Soc* **2002,** 124, 8546-7.
65. Li, R.; Chou, W. K.; Himmelberger, J. A.; Litwin, K. M.; Harris, G. G.; Cane, D. E.; Christianson, D. W. *Biochemistry* **2014,** 53, 1155-68.
66. Holm, L.; Rosenstrom, P. *Nucleic Acids Res* **2010,** 38, W545-9.
67. Krissinel, E.; Henrick, K. *Acta Crystallogr D Biol Crystallogr* **2004,** 60, 2256-68.
68. Grundy, D. J.; Chen, M.; Gonzalez, V.; Leoni, S.; Miller, D. J.; Christianson, D. W.; Allemann, R. K. *Biochemistry* **2016,** 55, 2112-21.
69. Baer, P.; Rabe, P.; Citron, C. A.; de Oliveira Mann, C. C.; Kaufmann, N.; Groll, M.; Dickschat, J. S. *Chembiochem* **2014,** 15, 213-6.
70. Harris, G. G.; Lombardi, P. M.; Pemberton, T. A.; Matsui, T.; Weiss, T. M.; Cole, K. E.; Koksal, M.; Murphy, F. V. t.; Vedula, L. S.; Chou, W. K.; Cane, D. E.; Christianson, D. W. *Biochemistry* **2015,** 54, 7142-55.